Local Magnitude (M_L) Calibration in the Short-Distance Range—The Case of the Collalto Seismic Network and Surrounding Stations in Northeastern Italy

Enrico Priolo*[1], Maria Adelaide Romano[1], and Laura Peruzza[1]

ABSTRACT

OPEN ACCESS

We calibrate local magnitude equations for northeastern Italy, centered on the Collalto seismic network, using the International Association of Seismology and Physics of the Earth's Interior (IASPEI) parametric formulation and a modified approach from Chovanová and Kristek (2018). Our goal is to develop an M_L distance correction well constrained at short distances, adhering to the Richter definition. Using digital data from 2012 to 2023, we find initial parameters similar to those obtained by Bragato and Tento (2005) on an independent dataset. These values differ significantly from the literature, but their physical meaning is questionable. We then introduce an additional procedural step to reduce the bias likely caused by data oversampling in the 10–40 km range. The resulting equations are $M_L^H = \mathrm{Log}A_H - (-1.545\mathrm{Log}(R/100) + 0.001357(R-100) - 3 + S_i^H)$ and $M_L^V = \mathrm{Log}A_V + 0.238 - (-1.555\mathrm{Log}(R/100) + 0.000995(R-100) - 3 + S_i^V)$ for the horizontal and vertical components, respectively; the S_i represent static corrections for each station and instrumentation configuration. Our new scale is valid for distances 7–200 km and magnitudes from −0.8 to 5.8. It aligns pretty well with the Hutton and Boore (1987) equation from 15 to 160 km, despite the different coefficients; below 50 km distance, where it is best constrained, it generally provides higher values than the other Italian laws and laws tuned for the shortest distances. Average residuals reveal a ± 0.1 perturbation between 40 and 170 km, closely matching a pattern found by Bragato and Tento as well. Our findings highlight the critical impact of distance oversampling and confirm a regional perturbation of wave propagation that affects the Wood–Anderson amplitudes. Our scale aligns linearly with independently calculated M_w and shows to be reliable for the investigated magnitude range across the whole regional area. Thus, it is usable by both local and regional networks in all of northeastern Italy.

KEY POINTS

- Using 2012–2023 data, we calibrate an M_L scale for NE Italy for distances 7–200 km and magnitudes −0.8 to 5.8.
- The new M_L equations address oversampling bias, regional attenuation, and station-specific corrections.
- Consistent with Richter's definition, the new scale performs reliably for dense local and regional networks.

Supplemental Material

INTRODUCTION

The steady increase in industrial activities that exploit the Earth's underground resources has led to the proliferation of dedicated seismic monitoring networks. These networks detect and locate weak earthquakes and microquakes, typically within a range of a few kilometers to a few tens of kilometers. "Industry-oriented" networks are more local and denser than those used for regional or national monitoring of natural seismicity. They are often deployed in populated areas, as industrial activities frequently occur there (e.g., enhanced geothermal projects near cities such as Pohang in South Korea, Strasbourg in France, or Basel in Switzerland). To date, several protocols and

1. National Institute of Oceanography and Applied Geophysics – OGS, Trieste, Italy, https://orcid.org/0000-0002-4392-6781 (EP); https://orcid.org/0000-0002-7191-0496 (MAR); https://orcid.org/0000-0001-7781-5775 (LP)

*Corresponding author: epriolo@ogs.it

Cite this article as Priolo, E., M. A. Romano, and L. Peruzza (2026). Local Magnitude (M_L) Calibration in the Short-Distance Range—The Case of the Collalto Seismic Network and Surrounding Stations in Northeastern Italy, *Bull. Seismol. Soc. Am.* **116**, 984–1006, doi: 10.1785/0120250059

regulations have been developed to provide guidelines for designing such monitoring networks and using data obtained from monitoring subsurface phenomena to prevent potentially dangerous earthquakes (e.g., Majer *et al.*, 2012; MiSE-UNMIG, 2014; Maury *et al.*, 2023). All these protocols require real-time seismic monitoring and quasi-real-time determination of seismological parameters.

Standard processing of seismic data acquired through dense networks allows for the estimation of event time, location, and magnitude. Additional parameters, such as corner frequency, seismic moment, and stress drop, can also be estimated depending on data quality. Magnitude and distance to industrial activities form the basis for protocols aimed at mitigating and managing induced seismicity, such as the well-known "traffic light system" (Bommer *et al.*, 2006; Majer *et al.*, 2012). Therefore, the accuracy of magnitude estimation at short distances (i.e., less than 10–15 km from a seismic station) is critically important, not only for scientific purposes but also for implementing effective management protocols.

The concept of the local magnitude scale (M_L) was introduced in the original study by Richter (1935), who established an empirical law valid for southern California that has been used worldwide for decades to measure the size of earthquakes at distances between 20 and 600 km. This formula defines M_L as a function of the maximum trace amplitude A_{max}, measured in millimeters and recorded by a Wood–Anderson standard torsion seismometer, corrected for a distance-dependent term, and it is usually known in the following form:

$$M_L = \mathrm{Log}A_{max} - \mathrm{Log}A_0(D), \quad (1)$$

in which D is the epicentral distance of the recording station.

Richter (1958) defines the term $-\mathrm{Log}A_0(D)$—today we call it the attenuation term—in tabular form in such a way that $M_L = 3$ if the recorded maximum amplitude is 1 mm for an earthquake at a distance of 100 km. The determination of the term $-\mathrm{Log}A_0(D)$ with such a convention is called magnitude calibration.

In the 1980s, Bakun and Joyner (1984) calibrated the M_L formula for central California, and Hutton and Boore (1987) re-evaluated it for southern California using much larger datasets. These studies were later adopted by the International Association of Seismology and Physics of the Earth's Interior (IASPEI) into the general log-linear formulation used worldwide

$$M_L = \mathrm{Log}A - (n\mathrm{Log}R + KR + C + S), \quad (2)$$

in which A is the Wood–Anderson horizontal displacement amplitude measured in nm, R is the hypocentral distance in km, n and K are coefficients normally related to geometrical spreading and intrinsic attenuation, respectively, C is a constant used to calibrate the formula to a reference value, and S is the station correction (Bormann, 2012).

Although many studies have been conducted to calibrate local magnitude at the regional or national level, very few studies have addressed the problem of estimating local magnitude at short distances (i.e., less than about 15 km), which is required for dense, industry-oriented networks.

For some events induced by hydraulic fracturing at the Preese Hall well near Blackpool, United Kingdom, Butcher *et al.* (2017) showed that the local magnitude calculated by the local monitoring network at short hypocentral distances was significantly higher than the magnitude estimated by the UK National Seismic Network stations, which were located at distances between 80 and 110 km. The authors attributed this discrepancy to the influence of sedimentary layers at the local scale that increase the amplitudes. Therefore, they recalculated the coefficients of the formula used at the national level (Ottenmöller and Sargeant, 2013) and defined a new formula that can be used locally for hypocentral distances in the 5–20 km range.

Luckett *et al.* (2019) added a new exponential term to the classical formula based on the observation that the single-station M_L calculated at stations less than 10 km away is up to one unit higher than the M_L calculated at the most distant stations; in this way, they reduced the scatter due to the unexpectedly high values at short hypocentral distances and allowed the use of a single formula for all distances. They applied this correction to datasets from the United Kingdom, Norway, and the 2016 Amatrice, Italy, seismic sequence and demonstrated the effectiveness of this approach for different areas. Remarkably, they acknowledge that the form of this additional term was chosen "simply because it describes the observed data," whereas "the underlying physical reason is not clearly understood."

In this work, we calibrate the local magnitude equation for the area monitored by the Collalto seismic network. This network has been operational since 2012 and monitors natural and potentially induced seismicity in the vicinity of the Collalto underground gas storage facility (Priolo *et al.*, 2015) in northeastern Italy (Fig. 1). We employ the general parametric formula for the magnitude proposed by IASPEI (Bormann *et al.*, 2012) and determine the best constants for our study area using a modification of the approach proposed by Chovanová and Kristek (2018) for Slovakia.

We deliberately adopt the standard IASPEI M_L formulation without introducing additional empirical distance-dependent correction terms (e.g., Luckett *et al.*, 2019) or resorting to a nonparametric formulation (e.g., Bragato and Tento, 2005; Lolli *et al.*, 2015), to preserve consistency with the internationally accepted definition of local magnitude and to ensure direct comparability with the practices adopted by the majority of authoritative seismic monitoring networks.

We use all the available digital data for the decade 2012–2023 from the Collalto seismic network, and from some stations of the northeast Italy (NEI) regional network managed by the National Institute of Oceanography and Applied Geophysics

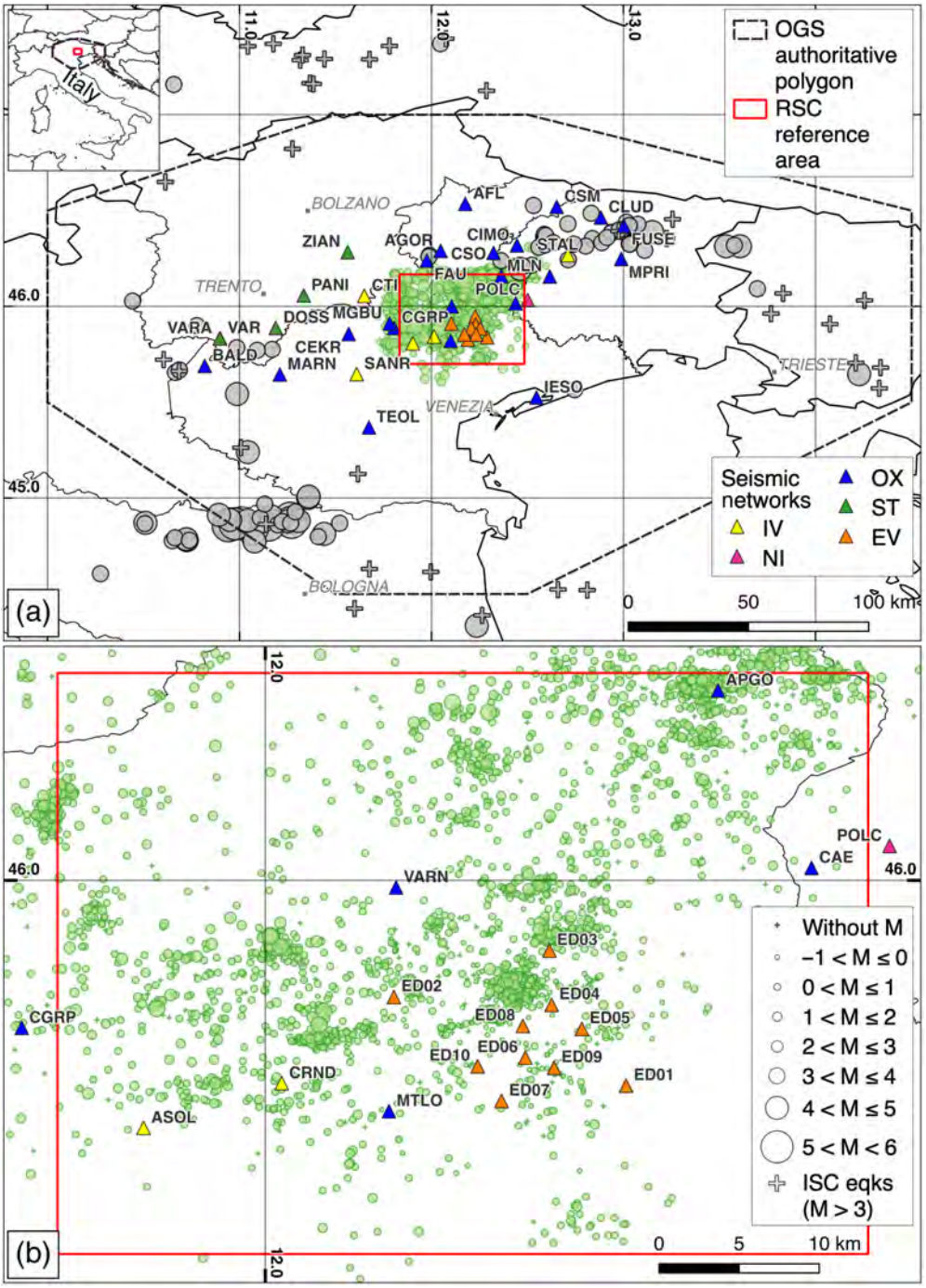

Figure 1. Map of the study area with the earthquakes and stations used. The inset in the upper left corner shows the location map of the study area within Italy. Panels (a) and (b) show the stations locations and two different groups of earthquakes from the entire earthquake dataset: regional earthquakes (gray symbols, panel a; circles and crosses represent the National Institute of Oceanography and Applied Geophysics [OGS] or National Institute of Geophysics and Volcanology [INGV], and International Seismological Centre [ISC] locations, respectively) and local earthquakes (green circles, panel b). The red rectangle in both panels (a) and (b) represents the reference area monitored by the Collalto network (Priolo *et al.*, 2015), and the polygon with the black dashed line encloses the authoritative seismic monitoring area of the OGS. The size of the earthquake symbols is proportional to the local magnitude as it appears in the original catalogs (see also the legend). The seismic stations (triangles) are colored according to the seismic network to which they belong to (see also the International Federation of Digital Seismograph Networks [FDSN] codes in the legend on the left): EV, Collalto Seismic Network; IV, Italian National Seismic Network; NI, northeast Italy Broadband Network; OX, northeast Italy Seismic Network; and ST, Trentino Seismic Network. The color version of this figure is available only in the electronic edition.

(OGS), with a maximum distance of about 250 km between earthquakes and stations; the earthquake catalog covers the magnitude range from M_L −0.8 to 5.8, and provides adequate distance/azimuth coverage for most of the stations. We compute Wood–Anderson amplitudes from the entire dataset of available full waveforms, and apply ad hoc developed pre- and postprocessing techniques to select the right signals and obtain reliable amplitudes even for noisy signals. Furthermore, some procedures are used to reduce erroneous amplitude values, inadequate azimuthal coverage, insufficient range coverage, and to test the statistical robustness of the results.

MAGNITUDE CALIBRATION: METHOD

The IASPEI Working Group on Magnitude Measurement recommends the following standard formula for calculating M_L for crustal earthquakes in regions with similar attenuation characteristics to southern California (Bormann, 2012):

$$M_L = \mathrm{Log}A + 1.11\mathrm{Log}R + 0.00189R - 2.09, \quad (3)$$

in which R is the hypocentral distance instead of the epicentral distance of the original Richter (1935) formula, and A, measured in nm, accounts for the correct Wood–Anderson seismograph response, that is, a static magnification of 2080 instead of 2800 and a damping factor of 0.7 instead of 0.8 (Uhrhammer and Collins, 1990). Thus, for $A = 10^6/2080$ nm and R = 100 km, equation (3) results in $M_L = 3$ (Havskov and Ottenmöller, 2010).

Note also that equation (3) can be expressed equivalently by explicitly specifying the reference distance at which the magnitude is calibrated, that is,

$$M_L = \mathrm{Log}A_{WA} + 1.11\mathrm{Log}(R/100) + 0.00189(R - 100) + 3.0, \quad (4)$$

in which A_{WA} accounts for the change of amplitude unit from nm to mm, 100 represents the reference hypocentral distance in km for which the maximum horizontal displacement of an original Wood–Anderson seismograph of 1 mm would be associated with an $M_L = 3$. Equation (4) is the form given by Hutton and Boore (1987), who also suggest using a shorter reference distance of 17 km to calculate the magnitude of earthquakes detected by local networks; at a hypocentral distance R = 17 km, an earthquake of magnitude $M_L = 2$ would result in A = 1 mm.

Equations (3) and (4) apply only to regions with attenuation characteristics similar to those of southern California, and they remain the standard practice for M_L computation in most seismological observatories worldwide. In regions with different attenuation properties, IASPEI guidelines leave the choice of the functional form of the equation and the constraints imposed on the fitted empirical parameters entirely open. Nevertheless, most authors have calibrated M_L using the general log-linear formulation given in equation (2). It is beyond the scope of this article to provide a detailed review of all the investigations conducted to calibrate M_L for different areas; instead, for the targets we are more interested in (i.e., short distances/small earthquakes, and northeastern Italy), we address:

- the works of Butcher *et al.* (2017) and Luckett *et al.* (2019), already mentioned in the introduction, because they extend M_L estimation to short distances; and
- the calibrations proposed for Italy by Spallarossa *et al.* (2002), Bragato and Tento (2005), Bobbio *et al.* (2009), and Di Bona (2016) for northwestern, northeastern, and southern Italy, respectively; and by Lolli *et al.* (2015) and Di Bona (2016) for the entire Italian territory.

To calibrate the local magnitude, that is, to perform a linear regression of equation (2), we initially adopt the method proposed by Chovanová and Kristek (2018)—a data-driven procedure organized in three consecutive steps—and implement it in a MATLAB code. After several sensitivity tests and validation of the inversion procedure using synthetic datasets, we add a fourth statistically driven step, aimed at reducing the bias caused by oversampled distances on the inversion results. The formalism of the method is as follows.

Let j and i be the indices from 1 to N_E and N_S for the earthquakes and the stations, respectively. Substituting the amplitude and distance data into equation (2) we obtain an overdetermined linear system of the form:

$$\mathrm{Log}A_{ji} = M_{Lj} + n\mathrm{Log}R_{ji} + KR_{ji} + S_i + C; j = 1,\ldots N_E; i = 1,\ldots N_S. \quad (5)$$

Because not all the stations record the same event, we indicate with N the total number of the available waveform amplitudes, that is, the Wood–Anderson simulated peak amplitudes. Because the magnitude of the jth event and the constant C are coupled, we cannot determine them separately. We then define

$$M_j = M_{Lj} + C, \quad (6)$$

and introduce it into the system (5), which gives us

$$\mathrm{Log}A_{ji} = M_j + n\mathrm{Log}R_{ji} + KR_{ji} + S_i; j = 1,\ldots N_E; i = 1,\ldots N_S. \quad (7)$$

We also impose the condition that the station coefficients (i.e., the static correction) give an average value of zero,

$$S_1 + S_2 + \ldots + S_{Ns} = 0. \quad (8)$$

The coefficient C and the station coefficients S_i will be solved in the final calibration step.

The linear system given by equations (7) and (8) is solved with the MATLAB operator "\", which provides the least-square solution that minimizes the residuals in the two-norm using a QR factorization (decomposition into an orthogonal matrix Q and an upper triangular matrix R).

The first step of the solution procedure aims to remove the outliers from the global linear system. Equations (7) and (8) are solved for the unknown parameters n, K, and S_i, and the residuals r_{ji} are calculated as

$$r_{ji} = \mathrm{Log}A_{ji} - (M_j + n\mathrm{Log}R_{ji} + KR_{ji} + S_i); j = 1,\ldots N_E; i = 1,\ldots N_S. \quad (9)$$

Outliers are defined as the data outside a quantity proportional to the interquartile range of the residuals (IQR). This step consists of an iterative process in which equation (9) is solved, IQR is estimated, outliers are removed from the dataset, and the linear system is updated with the remaining data for a new iteration step. Iteration stops when all outliers are removed from the dataset.

In the second step, a solution is found that minimizes the unbiased sample standard deviation of the residuals σ, which is defined as

$$\sigma = \mathrm{sqrt}((\Sigma r_{ij}^2)/(N - (N_E + N_S + 1))). \quad (10)$$

In this case, the best solution to the following equation:

$$\mathrm{Log}A_{ji} - n\mathrm{Log}R_{ji} - K\,R_{ji} = M_j + S_i, \quad (11)$$

is found through a local grid search in the space of parameters n and K, in a neighborhood of the final solution of the previous

step. In practice, given n and K, taken in the selected grid interval, we get residuals for calculating equation (10) by estimating M_j and S_i from equation (11) using regression analysis. The grid search can be repeated by changing the grid resolution to an acceptable value. The second step was applied iteratively (three iterations on average), starting from a coarser grid and refining it until the minimum was clearly identified. Given the simplicity of the misfit function and the limited dimensionality of the parameter space, this approach proposed by Chovanová and Kristek (2018) proved sufficiently accurate and robust, and no evidence of aliasing effects related to periodic noise was observed in the inversion results.

The third step determines the constant C and then the static station coefficients S_i. Assuming that $\overline{n}$ and $\overline{K}$ are the best solutions for n and K found after the previous step, the constant C is estimated as follows:

$$\overline{C} = -M_0 + \mathrm{Log}A_0 - \overline{n}\mathrm{Log}R_0 - \overline{K}R_0, \tag{12}$$

in which M_0 is the reference magnitude for which at a source–station distance R_0 a reference Wood–Anderson peak amplitude A_0 is found. Finally, the static station coefficients are calculated as follows:

$$S_i = \mathrm{Log}A_{ji} - (\overline{n}\mathrm{Log}R_{ji} + \overline{K} + R_{ji} + \overline{C}) - M_j, \tag{13}$$

together with condition (8).

We add a fourth, final, statistically driven step, aimed at reducing the bias of oversampled distances on the inversion results. To this end, we extract by random selection on the original data N_D subsets of amplitude/distance/station, with a more uniform distance distribution, and invert them. Then, the overall parameters n, K, and S_i are calculated as the mean of the individual parameters found for the N_D subsets.

We have verified the MATLAB code implementing the method of Chovanová and Kristek (2018) by some synthetic tests. We create synthetic amplitude datasets with the same distance and magnitude distributions of our original data (see subsequently in the text), using the parametric magnitude law developed by Di Bona (2016; see his equation 13) for Italy, namely:

$$M_\mathrm{L} = \mathrm{Log}A + 1.667\mathrm{Log}(R/100) + 0.001736(R-100) + 3, \tag{14}$$

as a reference for the calculation of WA synthetic amplitudes.

The first dataset contains the WA amplitudes calculated exactly by equation (14) from the original magnitudes. In the second and third datasets, the WA amplitudes are calculated after a perturbation is applied to the magnitudes, assuming a normal or a uniform distribution of the perturbation. Different datasets are created for the latter types to account for the different perturbation values (e.g., 0.3, 0.5 magnitude units). The results of the inversion show that the parameters n and K are accurately determined for the first dataset, whereas the accuracy of n and K coefficients decreases when the WA amplitude (or, equivalently, the reference magnitude) is increasingly perturbed. Further details are given in Text S1 of the supplemental material, available with this article.

STUDY AREA AND DATA

The area in which we have a statistically meaningful number of low-magnitude and short-distance earthquake recordings is in northeastern Italy, at the border between the southern Alpine front and the northern Veneto plain (Fig. 1, red rectangle).

From a tectonic point of view, this area is characterized by a west-southwest–east-northeast (WSW-ENE)-trending, south-southeast (S-SE) verging fold-and-thrust system, partly hidden under Quaternary sediments (Picotti *et al.*, 2022), and is undergoing an active shortening of ∼1 mm/yr in northwest–southeast (NW-SE) direction in response to the convergence between the Adria and Eurasia plates, as revealed by Global Positioning System (GPS) velocities (Anderlini *et al.*, 2020). The Parametric Catalog of Italian Earthquakes (CPTI15 v4.0; Rovida *et al.*, 2020, 2022) reports three main events in the study area: the Asolo earthquake (M_w 6.4) in 1695 in the southwestern corner, and two events in the Alpago-Cansiglio in the northeastern corner, one in 1873 with M_w 6.3 and one in 1936 with M_w 6.1. On the other hand, the seismic activity of the last fifty years, monitored at the regional scale by OGS, is quite moderate; the instrumental record shows only two dozen events with $M_\mathrm{L} > 3.0$ and a single event with $M_\mathrm{L} = 4.0$ occurred more than 40 yr ago (namely on 14 October 1980, see Sugan *et al.*, 2024; and Data and Resources).

In this area, OGS was commissioned by Edison Stoccaggio S.p.A. in 2010 to set up a dense local network for high-resolution seismicity monitoring around the "Collalto Stoccaggio" underground gas storage concession (Priolo *et al.*, 2015). The Collalto seismic network (RSC) began operating in 2011 and has been fully operational since 1 January 2012. It consists of ten seismic stations (orange triangles in Fig. 1, station codes ED01-ED10) and one permanent geodetic station at the ED06 site. The RSC is equipped with broadband seismometers, mostly deployed in boreholes at depths ranging from 5 to 155 m. Five stations are also equipped with accelerometers deployed at the ground surface. Real-time data acquisition, alerting, and automatic location of events are performed by the BRTT Antelope system. Signals are sampled at 200 Hz for the broadbands and 100 Hz for the accelerometers, then are transmitted to the OGS acquisition center, processed, and archived permanently in miniSEED format (Incorporated Research Institutions for Seismology [IRIS], 2012). Routine locations are performed using both Hypo71 (Lee and Lahr, 1975) and Hypoellipse (Lahr, 1999) codes. The first program provides locations consistent with those of the regional NEI seismic network managed by OGS, and the second provides more refined locations for studies of the seismicity and seismotectonics at the local scale. The local magnitude M_L indicated

in the RSC catalogs so far is estimated using the parametric attenuation law obtained by Bragato and Tento (2005) for northeastern Italy, and corrections to remove the static residuals of the stations derived empirically. The magnitude of completeness of the RSC network ranges from about 0.0 in the central part of the area up to 1.0 in the remaining parts. More details can be found in Priolo *et al.* (2015) and Romano *et al.* (2019).

The monitoring purposes of the local RSC network are enhanced by the real-time exchange of signals from some surrounding stations, which contribute to the automatic detection of events, discrimination between true/false events and local/regional/teleseismic events, automatic and manual relocation, and postprocessing. In particular, since 1977, the OGS has been managing the NEI regional seismic network (Priolo *et al.*, 2005; Bragato *et al.*, 2021); it alerts local civil protection authorities to regional events above the perception threshold (about M_L > 2.5) and publishes preliminary earthquake locations in quasi-real time on a dedicated website and on major social media, and revised bulletins later. The NEI network currently comprises 43 stations with a station spacing of about 15–40 km. The OGS also shares the signals of some stations in real time with the Italian nationwide seismic monitoring systems of the National Institute of Geophysics and Volcanology (INGV) (Rete Sismica Nazionale [RSN]; Michelini *et al.*, 2016), other regional data providers, and, at the international level, with the authorities of neighboring countries such as Slovenia and Austria.

For this study, we use data from the RSC network and some stations of the other networks, selected to extend the range of observations outside the core area, beyond the reference distance of 100 km, as local magnitude is by definition calibrated on observations at a distance of 100 km; we can thus provide the best constraints in a wider range of magnitude and distance applicable to northeastern Italy (Fig. 1).

Even if our analysis refers to the last twelve years, it is also worth remembering that the OGS network in NEI has crossed nearly all the technological changes in the seismological devices of the last 50 yr. Some articles have recalibrated the formulas used for magnitude assessment (see Moratto *et al.*, 2017; Sandron *et al.*, 2018, and references therein), and investigated the time–space variation of the magnitude of completeness (e.g., Gentili *et al.*, 2011; Peresan and Gentili, 2018). Nevertheless, a truly uniform measure of magnitude all over the decades is only partially reached.

The colored triangles in Figure 1 are the stations used to calibrate M_L in this study. The basic information on these stations is given in Table 1. Further information is in Text S2 and Table S2.

The earthquake data set used for M_L calibration at short distances is for the time period from 1 January 2012 to 31 March 2023, and consists of two groups as follows:

1. The entire RSC catalog in the previously quoted reference time frame (Fig. 1b); it contains 3491 earthquakes located by Hypoellipse and a custom velocity model estimated by Romano *et al.* (2019) in the reference area of the Collalto network (red rectangle in Fig. 1). For studying the impact of parsing the earthquake dataset on a priori rules, such as those based on location quality, the RSC catalog is subdivided in two separate data subsets. A first subset, containing the best-constrained hypocentral solutions (BC subset), has been built according to the following criteria (from Husen and Hardebeck, 2010): gap ≤ 180°; at least eight arrival times with at least one phase read at an epicentral distance less than or equal the hypocentral depth and one *S*-phase read at an epicentral distance less than or equal 1.4 times the hypocentral depth. The BC subset contains 1535 hypocentral solutions. The second subset contains all the remaining 1956 events.
2. A complementary list of 125 earthquakes selected from those recorded by the regional NEI network in the same period and located mainly (though not exclusively) far from the Collalto network, at distances of up to about 200 km (Fig. 1a). The minimum threshold in magnitude increases from 3 to 4, depending on the distance from the reference area. For this list of events, the hypocentral solutions are provided by different agencies, that is, OGS (mainly when epicenters fall within its authoritative polygon that covers Friuli Venezia Giulia, Veneto, and partially the Trento Province), INGV, and ISC (ISC epicenters shown by gray crosses in Fig. 1). No information about the contributing stations (i.e., arrival times) is easily accessible for this earthquake list.

The inclusion of events with larger magnitude and distances than the "core" dataset (e.g., $M_L > 5$ of the Emilia sequence) makes the calibration more robust and extends its range of validity. We are aware that the earthquake list used in this study is not uniform in terms of completeness, quality of hypocentral solutions, algorithm, and velocity model used for location, and estimation of the initial magnitude. A sensitivity analysis we performed on the effects of location error on the M_L estimates (see Text S3) shows that the geometric uncertainty has a negligible impact at large station–earthquake distances, of the order of 10^{-2} magnitude units for 1 km of mislocation at 100 km distance. The bias remains acceptable, up to about 10 km event–station distance, at about M_L 0.15 for 1 km of mislocation at 10 km distance. This location uncertainty component depends on the distance corrections, but always increases exponentially at very short distances (R < 5 km). In our case study, such very short distances are not represented in the dataset.

The data processing to calculate the Wood–Anderson peaks is as follows. For each earthquake, the raw waveforms from all available stations are extracted as a 240 s window with 40 s of pre-event signal before the event origin time t_0. In a preprocessing step, the signals are checked for possible fragmentation: small gaps are interpolated (SAC command *merge gap interp*),

TABLE 1
Overview of the Station Sites

Station Code	Net Code	Location	Longitude E (°)	Latitude N (°)	Elevation (m)	First Installation Date (yyyy/mm/dd)	Channel
AFL	OX	Alpe Faloria	12.1755	46.5283	2235	1995/01/01	SH, EH, HN
AGOR	OX	Agordo	12.0472	46.2829	631	2007/01/06	HH, HN
APGO	OX	Alpago	12.3630	46.1516	598	2017/04/15	EH, HN
ASOL	IV	Asolo	11.9023	45.8003	181	2011/01/17	HN
BALD	OX	Monte Baldo	10.8187	45.6830	1911	2007/11/08	HH, HN
CAE	OX	Caneva	12.4378	46.0089	870	1995/01/01	SH, HH, HN
CEKR	OX	Cima Ekar (Asiago)	11.5685	45.8492	1365	2019/04/01	EH, HN
CGRP	OX	Cima Grappa	11.8047	45.8806	1757	2005/04/21*	HH, HN
CIMO	OX	Cimolais	12.4448	46.3116	710	2005/04/21	HH, HN
CLUD	OX	Cludinicco	12.8814	46.4569	635	2011/02/15	HH, HN
CRND	IV	Cornuda	12.0131	45.8361	159	2011/11/04	HN
CSM	OX	Casera Mimoias	12.6515	46.5125	1635	1995/01/01	SH, HH, HN
CSO	OX	Casso	12.3228	46.2724	1060	1995/01/01	SH, EH, HN
CTI	IV	Castel Tesino	11.6497	46.0482	1180	2003/03/01	EH, HH
DOSS	ST	Dosso del Sommo	11.1884	45.8808	1660	2011/12/11	HH, HN
ED01	EV	Susegana Santa Lucia	12.2892	45.8346	54	2011/12/03	HH, EH, HN
ED02	EV	Farra di Soligo	12.1031	45.9057	205	2011/12/03	HH, HN
ED03	EV	Corbanese	12.2278	45.9429	235	2011/12/03	HH
ED04	EV	Santa Maria di Feletto	12.2295	45.8994	182	2011/12/03	HH
ED05	EV	San Michele di Feletto	12.2538	45.8801	110	2011/12/03	HH, HN
ED06	EV	Collalto Campo 6	12.2085	45.8570	174	2011/12/03	HH, HN
ED07	EV	Nervesa della Battaglia	12.1894	45.8222	167	2011/12/03	HH, HN
ED08	EV	Collalto Cucco	12.2065	45.8825	194	2011/12/15	HH, HN
ED09	EV	Susegana Castello	12.2315	45.8488	105	2011/12/03	HH
ED10	EV	Santa Croce del Montello	12.1702	45.8500	144	2011/12/03	HH
FAU	OX	Forcella Aurine	11.9753	46.2322	1430	1995/01/01*	SH
FUSE	OX	Fusea	13.0011	46.4142	520	2007/12/13	HH, HN
IESO	OX	Iesolo	12.5464	45.5178	0	2001/04/01	SH, EH, HN
MARN	OX	Marana	11.2099	45.6378	785	2009/11/24	HH, HN
MGBU	OX	Monte Grappa	11.7813	45.9041	1517	2022/05/01	HH, HN
MLN	OX	Malnisio	12.6154	46.1495	814	1995/11/02	SH, HH, HN
MPRI	OX	Monte Prat	12.9872	46.2400	762	1995/01/01	SH, EH, HH, HN
MTLO	OX	Montello	12.0991	45.8136	350	1995/01/01	SH, HH, HN
PANI	ST	Panarotta	11.3349	46.0508	1985	2008/01/01	EH, HN
POLC	NI	Polcenigo	12.5005	46.0266	150	2007/12/13	HH, HN
SANR	IV	Sandrigo	11.6099	45.6400	51	2012/01/23	HN
STAL	IV	Staligial	12.7104	46.2601	625	2010/05/25	HH, HN
TEOL	IV	Teolo	11.6740	45.3617	370	2002/03/06	SH, HH
VARA	ST	Varagna	10.8965	45.8260	1735	2012/11/19	EH
VARN	OX	Varnada	12.1048	45.9933	1265	2006/11/16	SH, HH, HN
ZIAN	ST	Ziano di Fiemme	11.5632	46.2764	1154	2012/11/19	EH

In the channel field, sensor types are defined according to the International Federation of Digital Seismograph Network (FDSN) channel convention (see Data and Resources).
*Cessation of operation.

whereas the signal is discarded if large gaps are found (usually the gaps are similar for all three components). A procedure was then implemented to calculate the Wood–Anderson (WA) maximum values from all available waveforms for all considered events. In the first step, the corresponding instrument correction is applied for each waveform, and the WA waveform is simulated (SAC command *transfer from polezero … to …*).

For simulating the WA response and restricting the larger band of the modern digital seismometers to that of the WA, the suggestions by Havskov and Ottenmöller (2010) and the IASPEI magnitude recommendations (Bormann *et al.*, 2012) are followed. We distinguish between weak events, for which the corner frequency lies within the plateau of the WA spectral response, and moderate events, which have relevant content of low frequencies. After a sensitivity analysis, we set the magnitude threshold of M_L 3.5 to apply different processing filters. In practice, we apply within the same SAC command the WA simulation—a phaseless band-pass filter applied to the displacement in the band 1.25–20 Hz—and a band-pass cosine taper to improve the signal-to-noise ratio (SNR), which

depends on the earthquake magnitude. The cosine tapers are 0.625–1.25 Hz and 20–40 Hz for $M_L < 3.5$, and 0.01–0.1 Hz and 20–40 Hz for $M_L \geq 3.5$. Text S4 shows some examples of the impact of the band-pass filter.

The maximum Wood–Anderson zero-to-peak amplitudes for all three components are measured in a precalculated time window that includes the approximate theoretical arrival times of the most energetic phases. Only signals for which the signal-to-noise ratio (SNR, defined as the ratio between the maximum WA amplitudes in the signal and noise windows) is above a certain threshold provide WA peaks to be further processed, whereas the others are discarded. Because the origin time t_0 of the event in the extracted waveforms is at 40 s, we define the noise window for the calculation of the SNR as [5, 35] s from the beginning of the waveform. The signal window is set to $[t_0 + t_P, t_0 + t_P + 3 * (t_R - t_P)]$ s, in which t_P and t_R are the theoretical travel times for the P and Rayleigh waves, respectively, and $t_0 = 40$ s. The SNR thresholds for retaining the WA peak calculations are set to 1.53 and 2.5, respectively, for the waveforms with a measured P-wave arrival time (according to the location details given in the RSC catalog), and for all other waveforms. These two thresholds were determined empirically after several tests during which we also checked that the dominant period of the signals is smaller than the dominant period of the noise, a condition for ensuring accurate signal amplitude measurements. They have been demonstrated to be effective for removing most of the spurious amplitudes. Some examples of the results of this step are shown in Figure 2.

A further cleaning of the dataset is performed manually to remove spurious peaks not caused by earthquakes, as identified by anomalies in the Log(A) versus distance diagram, or by inconsistencies between WA waveforms' amplitudes derived from simultaneous recordings by colocated seismometers and accelerometers. We point out that this last step is possible because we identify each station configuration with great care, as described subsequently. Finally, data with very large residuals after the iterations of the first step of the inversion are also identified, checked, and eventually removed.

In real networks, even if the monitoring site coordinates remain the same, the technical characteristics of stations change over time. Sometimes these changes are not limited to the mechanical/electronic devices, but affect the deployment of sensors (e.g., depth or sensor coupling to the ground). In addition, some stations often have more than one sensor, for example, a seismometer and an accelerometer. Because we want to use all available data coming from different instruments and installations, these changes cannot obviously be mixed; thus, we have: (1) carefully traced the different instrument configurations, and (2) identified the time periods in which a given station maintains the same configuration. To distinguish the records, we append a letter to the original station code, so that the different configurations of the "same" station can be identified (see Text S2 for more details). These new station codes are used in the regression process. In this way, for each uniform station configuration, an independent station correction S_i is obtained from equation (2).

To our knowledge, no previous study has ever explored the consequences of such changes in the station correction parametrization; nonetheless, we acknowledge that detailed "station books", that is, the record of all the changes in station configuration, are not always available. We consider these records fully reliable for the RSC stations (network code EV), and for some NEI stations (network code OX). This approach offers several advantages, such as the possibility to evaluate the amplitude consistency between different configurations, the possibility to detect erroneous instrumental response functions used for instrument correction, and the retention of different configurations (e.g., a change in sensor depth) without affecting the overall regression. Conversely, the disadvantage is that a comprehensive, time-dependent station characterization has to be entered for the computation of magnitudes. All these aspects will be commented on later in the Discussion section.

The result of the processing described earlier is a huge table of three-component peak amplitudes with accompanying SNR values, station names, hypocentral distances, and some ancillary information about the related earthquakes. These data are used in the calibration procedure.

Figure 3 shows the distribution of the entire WA amplitude dataset in relation to (1) the source-receiver hypocentral distance, and (2) the magnitude values provided by the authoritative agency. The dataset consists of 36,225 station records with WA peak amplitudes; note that WA amplitudes may not be available for all three components. The hypocentral distances range from 2.8 to 295 km, with a median value of 24.5 km. The 5th–95th percentiles are 10.5–143.5 km. There are about 1200 observations for distances below 10 km. The magnitude values range from −0.8 to 5.8, with a median value of 0.95 and 5th–95th percentiles of 0.05–3.75. Note that the magnitude–frequency distribution does not follow a usual G-R pattern as completeness varies spatially.

RESULTS

The first step of the regression begins with a data set consisting of 34,805 and 28,038 WA peak amplitudes for the horizontal and vertical components, respectively. Following the Richter specification for the individual processing of the two horizontal components, and taking into account that the magnitudes of the two horizontal components have the same attenuation term, we calculate

$$\mathrm{LogWA}_H = 0.5(\mathrm{LogWA}_X + \mathrm{LogWA}_Y), \qquad (15)$$

and use WA_H for the inversion. If only one horizontal component is available, that value is used. The threshold for removing outliers was set to 1.8 times the interquartile range (IQR) for both components. After 19 and 15 iterations, respectively,

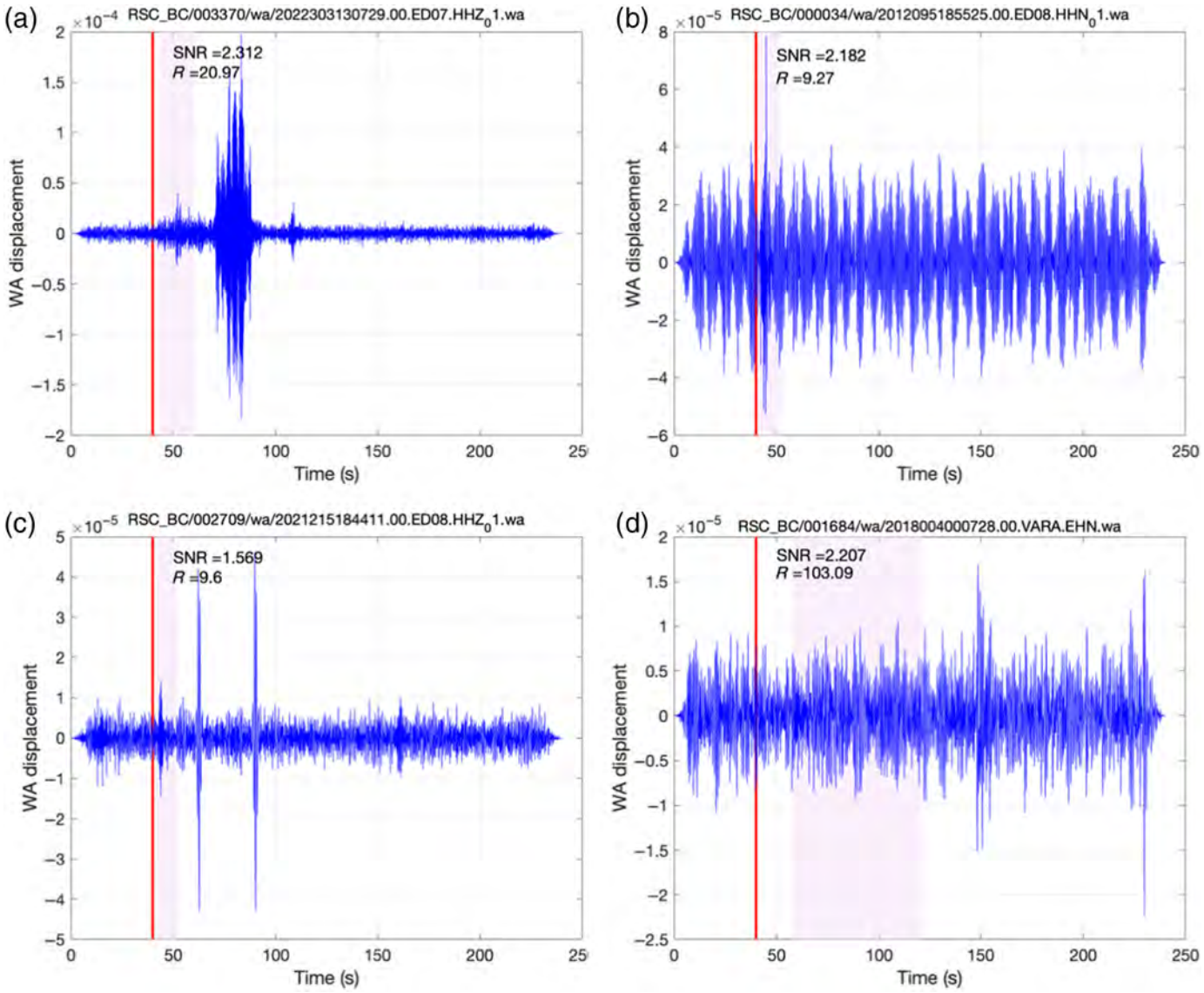

for the horizontal and vertical components, 3,006 and 2,592 outliers are removed, resulting in an input dataset for step 2 with 31,799 and 25,446 amplitudes belonging to 3,405 and 3,302 earthquakes. Figure 4 shows a summary plot of the dataset at the first and the last iteration. The figure also shows that the threshold for the outliers has changed (i.e., decreased) with the iterations. For example, for the horizontal component, it starts at 0.4644 for the first iteration and ends at 0.3525 for the last iteration. The parameters n and K obtained at the end of the first step are $(n,K)_H = (-2.262,0.004265)$ and $(n,K)_V = (-2.346,0.004476)$.

The grid search of the second step is performed with ranges/grid increments of -2.220 to $-2.206/2.0 \times 10^{-4}$ and $0.0041–0.00422/3.0 \times 10^{-6}$ for the horizontal component. The final (i.e., best) values found for the two components are: $(n,K)_H = (-2.212,0.004168)$ and $(n,K)_V = (-2.346,0.004475)$.

The coefficients n and K determined so far differ from those proposed for California or the entire Italian territory.

Figure 2. Examples of simulated Wood–Anderson recordings. The red line represents the origin time t0 (40 s after the start of the waveform), the reddish shadow shows the time window of theoretical arrivals of the most energetic phases, based on station–hypocenter distance and a simplified constant velocity model; the estimated signal-to-noise ratio (SNR) values and the hypocentral station–event distance R are listed in the upper left part of each frame. (a) A small event at about 21 km distance from the station, followed soon after by another stronger event. The SNR is about 2.3, and the peak amplitude is correctly identified. (b) Small event, embedded in a strong periodic component of ambient noise, with a manual P-phase arrival-time pick. The WA peak is clearly recognizable. The SNR is 2.18. (c) Small event with P-wave time pick embedded in ambient noise and with two other pronounced signals shortly after the theoretical arrival window. The waveform of the event is only faintly recognizable. The SNR is about 1.57. (d) Small event at about 100 km distance, embedded in the ambient noise, with no pick. The waveform of the event is not clearly recognizable. The SNR is about 2.2. This example represents the case of a doubtful event with the highest SNR value in the group of events without manual picks; the peak amplitude was discarded. The color version of this figure is available only in the electronic edition.

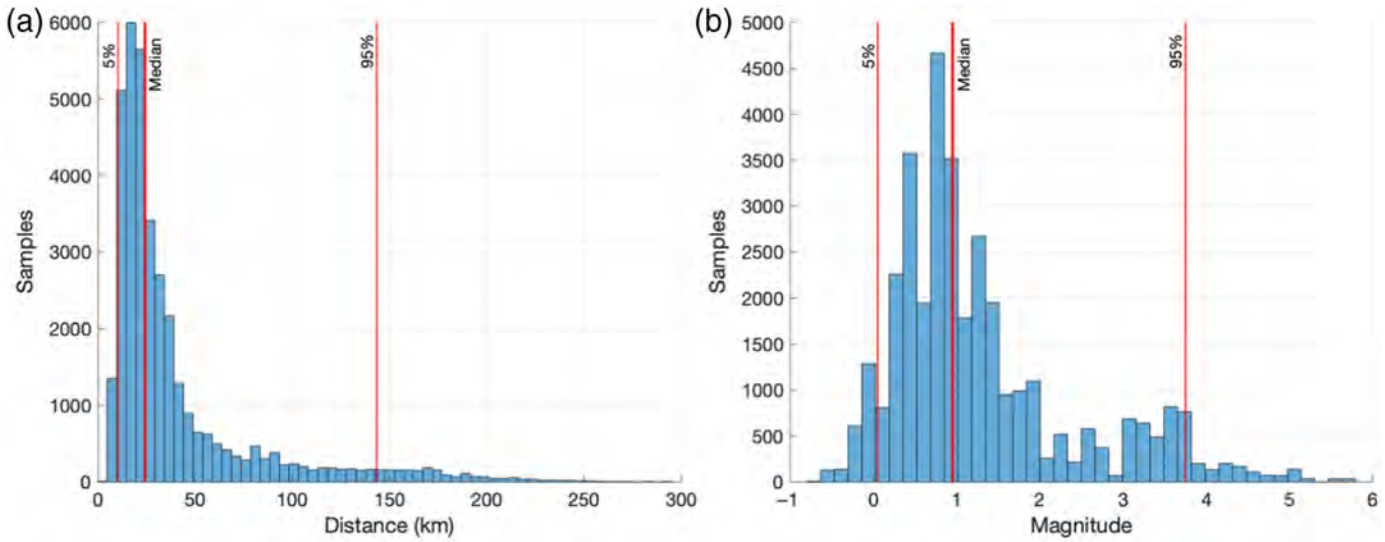

Figure 3. WA amplitude data set: (a) hypocentral distance distribution; (b) earthquake magnitude distribution. Each panel also shows the median value and the 5th and 95th percentiles of the distribution. The color version of this figure is available only in the electronic edition.

Specifically, our values for n are significantly lower—typically ranges are between −1.1 and −1.8—and the sign of K is reversed. In contrast, our coefficients closely align with those determined by Bragato and Tento (2005) for the horizontal component, which are n = −2.23 and K = 0.0039. Their 2005 study covered a similar geographic region but used a completely different dataset: earthquakes from 1995 to 2002, primarily located in Friuli and Slovenia; our analysis uses events from 2012 to 2023, mostly located in the Veneto and Friuli regions. In addition, the two studies rely on different groups of recording stations and instrumentation. Bragato and Tento performed a nonparametric inversion to determine the attenuation term $-\mathrm{Log}(A_0)$ and showed that it exhibits a complex behavior that the parametric inversion could not reproduce.

In the present study, after having verified the codes with synthetic datasets, as described in the Magnitude Calibration: Method section, we also performed an inversion using the best-constrained locations of the Collalto network only (BC dataset; see the Study Area and Data section), which consists of 17,510 observations, predominantly within distances below 80 km. The n and K coefficients we obtained from this test (namely $(n,K)_H = (-3.055,0.0143)$) indicate an even more pronounced divergence from common values. We thus hypothesize that the drift toward anomalous n and K coefficients, although it could be affected by wave propagation properties through the upper crust, may be strongly influenced by the nonuniform distribution of data points across distance ranges. As clearly illustrated in Figure 3, the number of amplitudes at 10–40 km distance is ten to twenty times greater than the ones at distances >60 km. Figure 5 clearly shows how the parameters n and K influence the theoretical curve of the $-\mathrm{Log}A_0(R)$ term, in two distinct distance ranges; n primarily dominates in the 0–70 km range (Fig. 5a), whereas K becomes dominant at distances beyond approximately 100 km, causing the curve to bend (upward for concordant sign of n and K, downward if reverse, Fig. 5b). We stress that Figure 5 is intended solely for illustrative purposes to show the results of a sensitivity analysis; the curve labeled as "Global Inversion" represents our intermediate result of the global inversion, which is physically implausible.

Thus, as previously mentioned, we introduce a fourth, statistically driven step to reduce the bias caused by the oversampling of distances in the inversion results. By a Monte Carlo-based subsampling approach, we create several datasets with a more uniform distance distribution by randomly selecting amplitudes from the original dataset and performing separate inversions on each selection. Specifically, we parse the distances into 60 linear bins in the range of 0–300 km and form 30 different datasets by random sampling, imposing an upper threshold of 200 samples per bin. Figure 6 provides an example of one such subset.

For the 30 datasets with random search of a more uniform distance distribution, we obtain 30 (n, K) solutions, for both the horizontal and vertical components; we then calculate their mean and standard deviation, which turn out to be

$$(\overline{n},\overline{K})_H = (-1.545 \pm 0.072635, 0.001357 \pm 0.000249), \quad (16)$$

$$(\overline{n},\overline{K})_V = (-1.555 \pm 0.075095, 0.000995 \pm 0.000266). \quad (17)$$

By imposing $M_L = 3$ for a Wood–Anderson peak amplitude of 1 mm at a distance of 100 km, we obtain the final equations for the horizontal component, which can be written as

$$M_L^H = \mathrm{Log}A_H - (-1.545\mathrm{Log}(R/100) + 0.001357(R-100) - 3 + Si), \quad (18a)$$

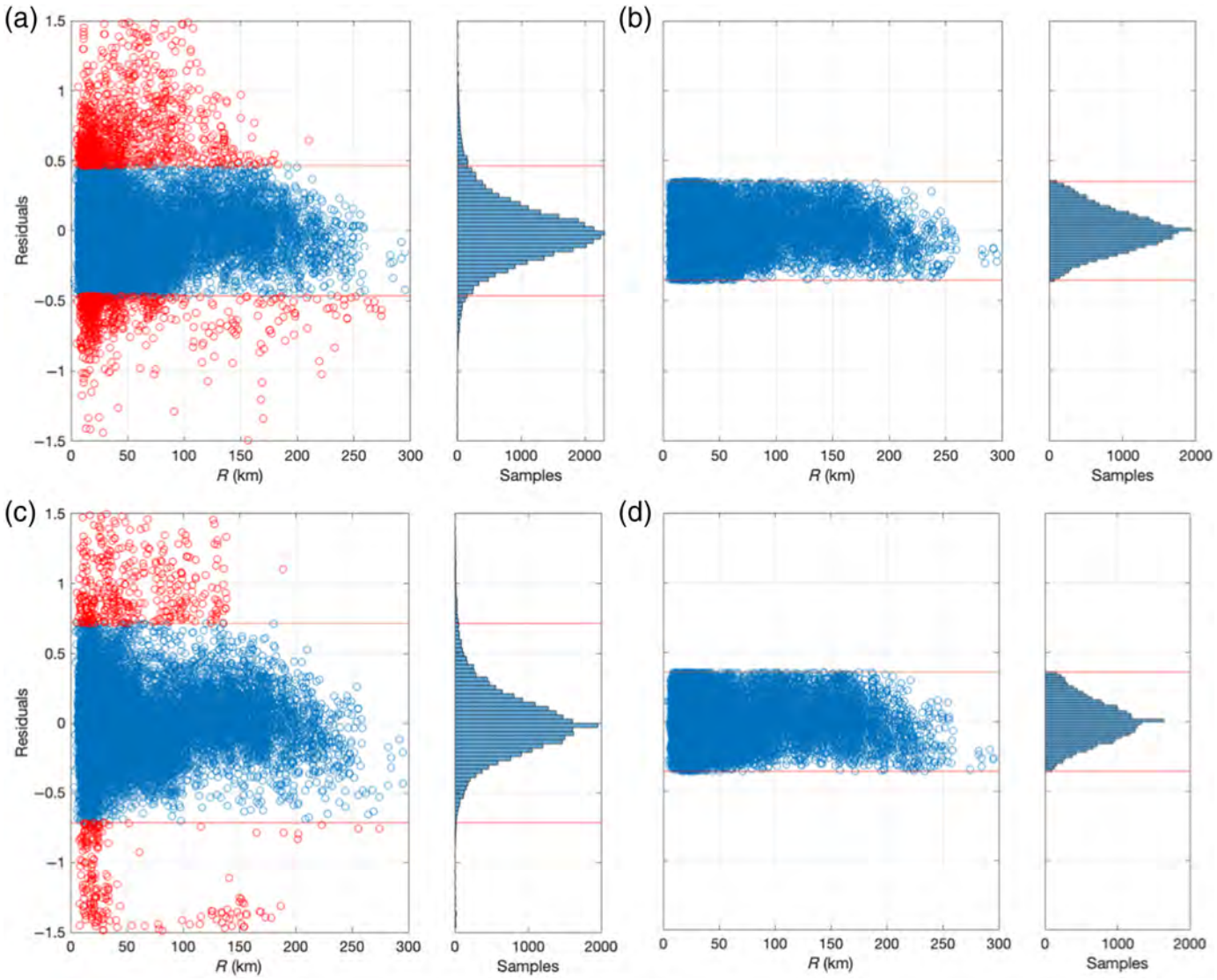

Figure 4. Distribution of station magnitude residuals as a function of distance. (a,b) and (c,d) refer to the horizontal and vertical components, respectively. On the left (a, c), the distribution of residuals for the entire data set at the first iteration; on the right (b, d) at the last iteration (i.e., when all outliers have been removed) for the refined data set. The circles represent the residuals, with those that lie within the predefined limits in blue and the outliers in red; the horizontal red lines represent the limits that are set at 1.8 of the interquartile range (IQR) of the residual distribution at the current iteration. The color version of this figure is available only in the electronic edition.

or, alternatively,

$$M_{\mathrm{L}}^{H} = \mathrm{Log}A_H - (-1.545\mathrm{Log}R + 0.001357R - 0.0457 + Si), \tag{18b}$$

in which A_H represents the horizontal Wood–Anderson amplitude expressed in mm, R is the hypocentral distance in km, and S_i represents the static station coefficient used for calculating the station–M_{L} for the ith station. Table 2 and Figure 7 show the static station coefficients S_i obtained at the end of the calibration for the latest station configuration (the complete list of coefficients is given in Table S2).

For the vertical component, the coefficient C is calculated differently because it is incorrect to normalize the equations for both components by imposing the same condition, given that the peak amplitudes on the vertical components tend to be smaller than those on the horizontal components. Considering that the attenuation properties (n, K coefficients) obtained for the global and decimated inversions are almost identical for the vertical and horizontal components, we verify that the amplitude ratio H/V has an almost constant value with distance, and then estimate it to be 1.73 (see details in Text S5). Thus, the vertical-component equations need an additional correction term equal to $\mathrm{Log}(H/V) = 0.238$, resulting in

$$M_{\mathrm{L}}^{V} = \mathrm{Log}A_V + 0.238 - (-1.555\mathrm{Log}\left(\frac{R}{100}\right) + 0.000995(R - 100) - 3 + Si), \tag{19a}$$

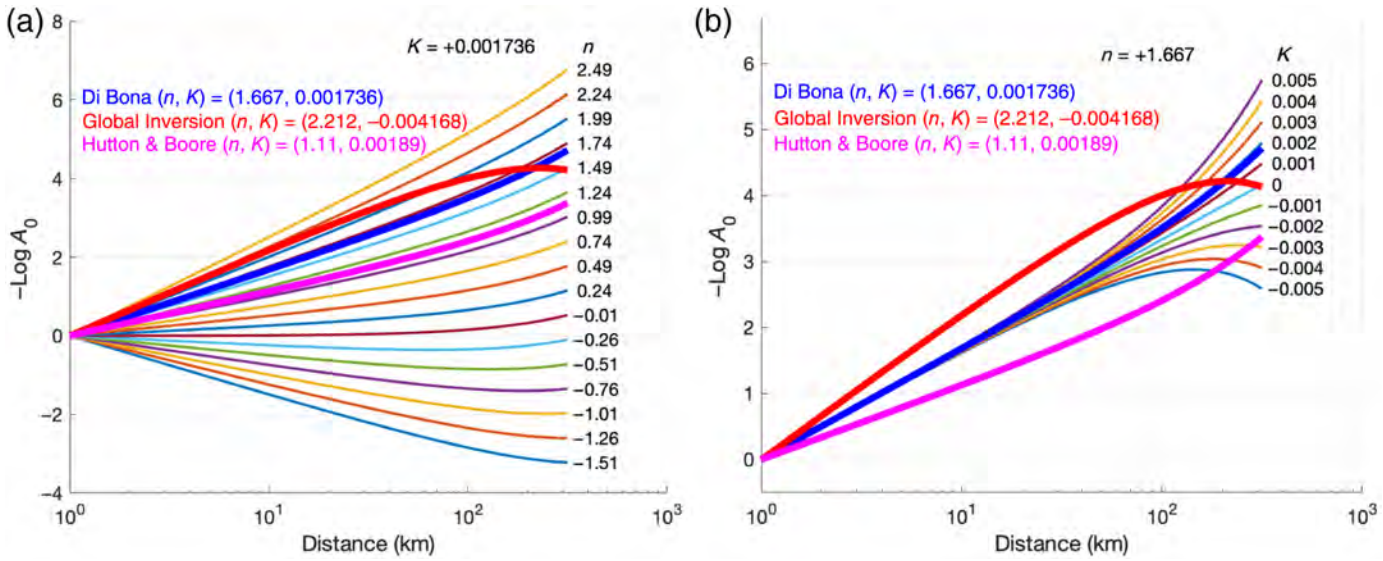

Figure 5. Sensitivity analysis of the n and K parameters. The panels represent the theoretical shape of the term minus Log$A_0(R)$. (a) Varying n for fixed K = +0.001736; (b) varying K for fixed n = +1.667. The numbers to the right of each curve indicate the value of the varying parameter (n for panel a and K for panel b). The fixed reference values used in the two panels are the coefficients of the magnitude law by Di Bona (2016). The thick lines in both panels represent the magnitude laws by Di Bona (2016) in blue, Hutton and Boore (1987) in magenta, and the value obtained in this study for global inversion of the entire dataset in red. The color version of this figure is available only in the electronic edition.

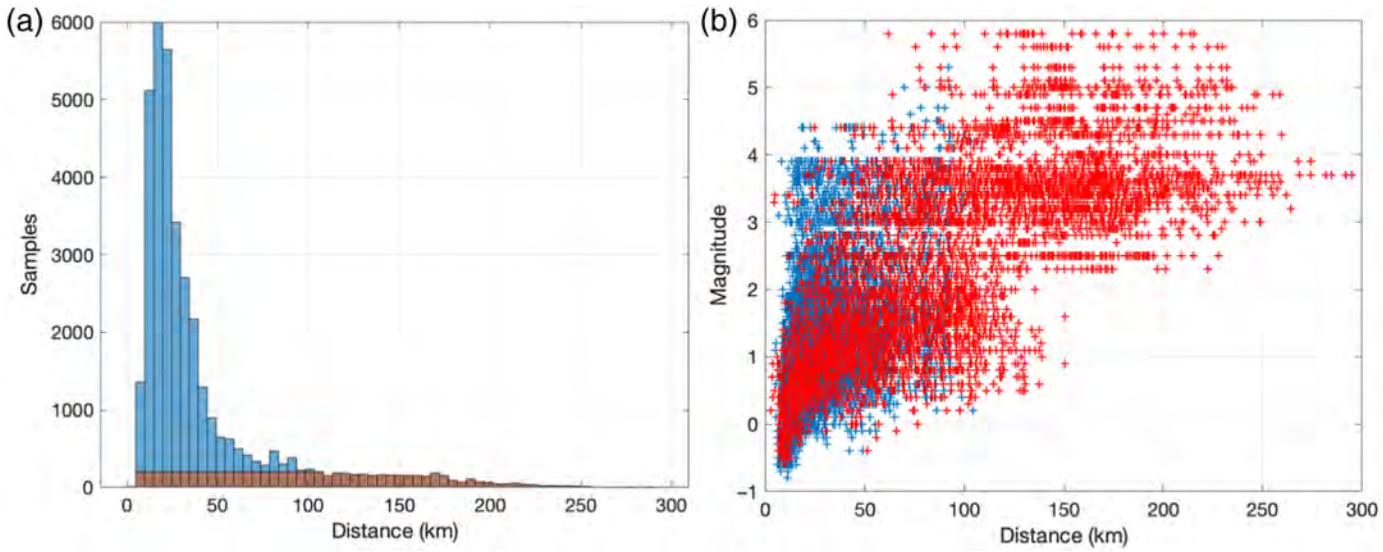

Figure 6. Example of a decimated subset versus the original dataset over distance. (a) Sample histogram versus distance of the original dataset (blue) and the decimated subset (brown). (b) Original magnitude versus distance of the initial dataset (blue crosses) and a decimated subset (red). The color version of this figure is available only in the electronic edition.

or, alternatively,

$$M_L^V = \mathrm{Log}A_V - (-1.555\mathrm{Log}R + 0.000995R + (0.0105 - 0.238) + Si). \quad (19b)$$

The first thing one can note in Figure 7 is that static station coefficients are within ±0.6, with most between ±0.4, a range which is in agreement with Bormann (2012). Another observation is that there is generally good agreement between configurations consisting of a seismometer and accelerometer deployed close to each other (e.g., BALD and BALD_z, CGRP and

TABLE 2
Static Station Coefficients for the Latest, Current Station Configuration; Two Codes in Case of Double Sensor

Station Code	Net-Code	Current Code	Sensor Type	Simplified Site Geology	S_i Horizontal Previous	S_i Horizontal New	S_i Vertical New
AFL	OX	AFL_b	Seism.	Dolostones, shallow water carbonatic platform, Upper Triassic	n.a.	−0.301	−0.2404
AGOR	OX	AGOR_b	Seism.	Bioclastic limestones, Upper Permian	−0.133	−0.199	−0.193
		AGOR_y	Acc.			−0.142	−0.131
APGO	OX	APGO_b	Seism.	Fluvioglacial and alluvial sediments of the mountains	n.a.	+0.477	+0.553
ASOL	IV	ASOL	Acc.	n.a.	n.a.	−0.264	−0.339
BALD	OX	BALD	Seism.	Micritic limestones, basins deposits, Jurassic–Cretaceous	+0.62	+0.464	+0.227
		BALD_z	Acc.			+0.441	+0.237
CAE	OX	CAE_c	Seism.	Micritic limestones, basins deposits, Jurassic–Cretaceous	+0.10	−0.198	−0.261
		CAE_z	Acc			−0.134	−0.250
CEKR	OX	CEKR_a	Seism.	n.a.	n.a.	−0.286	−0.193
CGRP	OX	CGRP	Seism.	Micritic limestones, basins deposits, Jurassic–Cretaceous	n.a.	−0.008	−0.161
		CGRP_x	Acc.			−0.024	−0.101
CIMO	OX	CIMO_b	Seism.	Dolostones, shallow water carbonatic platform, Upper Triassic	−0.24	−0.507	−0.323
		CIMO_y	Acc.			n.a.	n.a.
CLUD	OX	CLUD	Seism.	Massive dolostones and dolomitic limestones, Lower-Medium Triassic	−0.32	−0.468	−0.080
		CLUD_z	Acc.			−0.491	−0.127
CRND	IV	CRND	Acc.	n.a.	n.a.	−0.514	−0.677
CSM	OX	CSM_d	Seism.	Fluvioglacial and alluvial sediments of the mountains	−0.1	−0.225	−0.160
		CSM_z	Acc.			−0.115	−0.110
CSO	OX	CSO_d	Seism.	Fluvioglacial and alluvial sediments of the mountains	−0.3	−0.451	−0.310
		CSO_z	Acc.			n.a.	n.a.
CTI	IV	CTI_c	Seism.	n.a.	n.a.	+0.112	−0.007
DOSS	ST	DOSS	Seism.	Micritic limestones, basins deposits, Jurassic–Cretaceous	+0.08	+0.055	+0.052
		DOSS_z	Acc.			n.a.	n.a.
ED01	EV	ED01_f	Seism.	Fluvioglacial and alluvial sediments of the alluvial plain, Quaternary	+0.13	−0.033	−0.106
		ED01_x	Acc.			−0.044	−0.134
ED02	EV	ED02_f	Seism.*	Polygenic and heterometric conglomerates, marls, and siltstones, Plio-Quaternary	−0.04	−0.165	+0.218
ED03	EV	ED03_g	Seism.*	Polygenic and heterometric conglomerates, marls, and siltstones, Plio-Quaternary	+0.17	−0.124	+0.392
ED04	EV	ED04_d	Seism.*	Polygenic and heterometric conglomerates, marls, and siltstones, Plio-Quaternary	+0.32	+0.120	+0.407
ED05	EV	ED05_d	Seism.*	Polygenic and heterometric conglomerates, marls, and siltstones, Plio-Quaternary	+0.29	+0.020	+0.033
		ED05_z	Acc.			+0.161	+0.134
ED06	EV	ED06_h	Seism.*	Polygenic and heterometric conglomerates, marls, and siltstones, Plio-Quaternary	+0.33	+0.229	+0.038
		ED06_s	Acc.			+0.240	+0.044
ED07	EV	ED07_e	Seism.*	Polygenic and heterometric conglomerates, marls, and siltstones, Plio-Quaternary	+0.29	+0.118	−0.021
		ED07_s	Acc.			+0.303	+0.038
ED08	EV	ED08_g	Seism.*	Polygenic and heterometric conglomerates, marls, and siltstones, Plio-Quaternary	+0.17	+0.023	+0.414
		ED08_x	Acc.			+0.204	+0.090
ED09	EV	ED09_g	Seism.*	Polygenic and heterometric conglomerates, marls, and siltstones, Plio-Quaternary	+0.23	−0.056	−0.068

(*continued*)

TABLE 2 (*Continued*)

Station Code	Net-Code	Current Code	Sensor Type	Simplified Site Geology	S_i Horizontal Previous	S_i Horizontal New	S_i Vertical New
ED10	EV	ED10_f	Seism.*	Polygenic and heterometric conglomerates, marls, and siltstones, Plio-Quaternary	+0.23	−0.081	+0.272
FAU	OX	FAU	Seism.	Basement, paragneiss, and schists, pre-Paleozoic	−0.16	−0.187	−0.120
FUSE	OX	FUSE	Seism.	Massive dolostones and dolomitic limestones, lower-medium Triassic	−0.24	−0.286	−0.184
		FUSE_z	Acc.			−0.270	−0.179
IESO	OX	IESO_c	Seism.	Fluvioglacial and alluvial sediments of the alluvial plain, Quaternary	+0.64	+0.485	+0.386
		IESO_z	Acc.			n.a.	n.a.
MARN	OX	MARN	Seism.	Volcanic rocks (basalts, ignimbrites) Oligocene	+0.29	+0.276	+0.189
		MARN_z	Acc.			+0.201	+0.153
MGBU	OX	MGBU	Seism.	n.a.	n.a.	−0.149	−0.085
		MGBU_z	Acc.			n.a.	n.a.
MLN	OX	MLN_b	Seism.	Micritic limestones, basins deposits, Jurassic–Cretaceous	−0.19	−0.369	−0.244
		MLN_z	Acc.			−0.279	−0.125
MPRI	OX	MPRI_c	Seism.	Micritic limestones, basins deposits, Jurassic–Cretaceous	+0.21	−0.194	−0.244
		MPRI_z	Acc.			−0.142	−0.143
MTLO	OX	MTLO_d	Seism.	Sandstone-shale alternation (Flysch), Paleocene–Eocene	+0.58	+0.338	+0.073
		MTLO_x	Acc.			+0.331	+0.109
PANI	ST	PANI_b	Seism.	Basement, paragneiss, and schists, pre-Paleozoic	−0.15	−0.146	−0.122
		PANI_z	Acc.			n.a.	n.a.
POLC	NI	POLC	Seism.	n.a.	+0.38	+0.129	+0.050
		POLC_z	Acc.			n.a.	n.a.
SANR	IV	SANR	Acc.	n.a.	n.a.	−0.167	−0.397
STAL	IV	STAL_a	Seism.	n.a.	n.a.	−0.011	−0.075
		STAL_z	Acc.			n.a.	n.a.
TEOL	IV	TEOL_d	Seism.	Sandstone-shale alternation (Flysch), Paleocene–Eocene	+0.58	+0.423	+0.342
VARA	ST	VARA	Seism.	Micritic limestones, basins deposits, Jurassic–Cretaceous	n.a.	+0.453	+0.360
VARN	OX	VARN_e	Seism.	Micritic limestones, basins deposits, Jurassic–Cretaceous	+0.24	+0.098	−0.164
		VARN_x	Acc.			+0.107	−0.168
ZIAN	ST	ZIAN_a	Seism.	Volcanic rocks (basalts, ignimbrites), Oligocene	+0.16	−0.117	+0.058

The simplified site geology information is taken from Klin *et al.* (2021). Previous static station coefficients are the ones used for magnitude calculation in the Collalto network catalog (Priolo *et al.*, 2015). The complete list of instrument configurations and static station coefficients for the period considered in this study is listed in Table S2.
*Borehole Deployment.

CGRP_x, MTLO_d and MTLO_x, and VARN_e and VARN_x, as well as others). For the stations of the Collalto network (code ED##), we note, in Table 2 and Table S2, that the corrections estimated for the seismometers deployed in boreholes are lower than those of the corresponding accelerometer, if available. Unfortunately, some stations of this network have had a troubled life, with malfunctions of borehole sensors that have been replaced temporarily by surface sensors. This is the case for stations ED01, ED02, ED04, and ED05, where we can see a marked variability of values related mainly to the depth at which the sensor is deployed. For example: for ED01_d, ED01_e, and ED01_f which have the sensor at −153, −34, and 0 m, respectively, we have values of −0.336, −0.202, and −0.033; for ED04_b and ED04_c, which are installed at surface, we have values of approximately +0.4, whereas for ED04_a and ED04_d, which are at 27 m of depth, we have values of approximately +0.12. These observations are consistent with the expectation of more ground-motion amplification near or at the ground surface: the smaller the value of S_i, the lower the amplification at the station. It is also worth noting that values of S_i approaching zero do not necessarily correspond to "neutral," that is, nonamplifying, sites; this is the result of the 0-sum condition of equation (8), due to the station group used for calibration. Figure S4 shows the spatial distribution of the latest S_is. However, any interpretation of its physical meaning needs additional investigation and data that are out of the scope of this work.

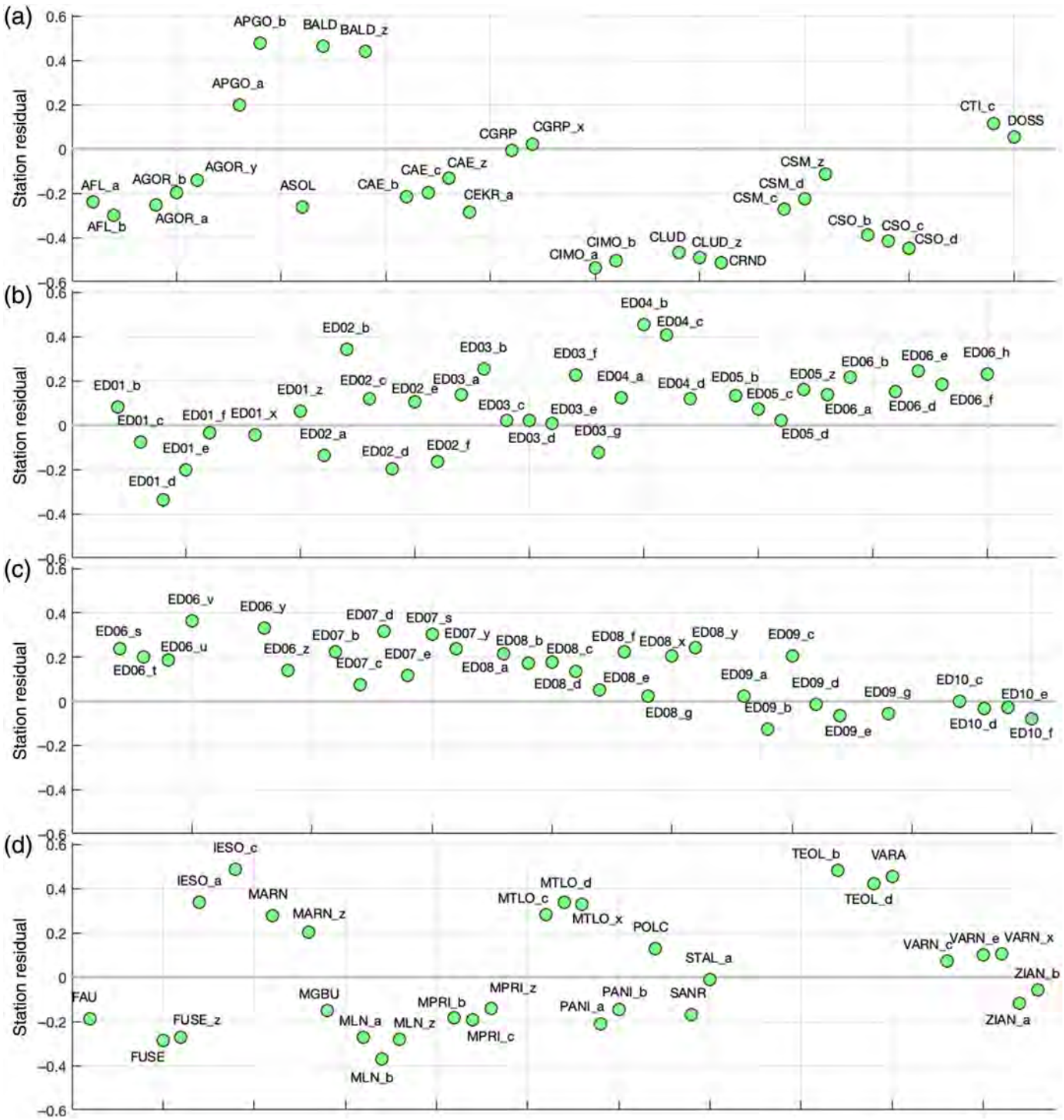

Figure 7. Static station coefficients calculated in this study for the horizontal component (S_i in equation 5), grouped alphabetically in four panels. Each station can have different configurations, as indicated by a supplementary letter after the station code (e.g., CODE_a). Seismometers have subsequent configurations labeled by ascending letters, starting with _a; accelerometers with descending letters, starting with _z. The complete list of station configurations is given in Table S2. The color version of this figure is available only in the electronic edition.

DISCUSSION

In the following, the results are discussed only for the horizontal component.

Figure 8 shows the newly obtained M_Ls compared with the previously available magnitudes. In Figure 8a, the single-station M_L values are plotted versus station distances; events with $2 < M_L < 3$ at distances greater than 100 km are less represented because they are not present in the RSC catalog, and the events that we used from other catalogs are all of M_L 3.0 or larger. Figure 8b compares the single-station M_L values

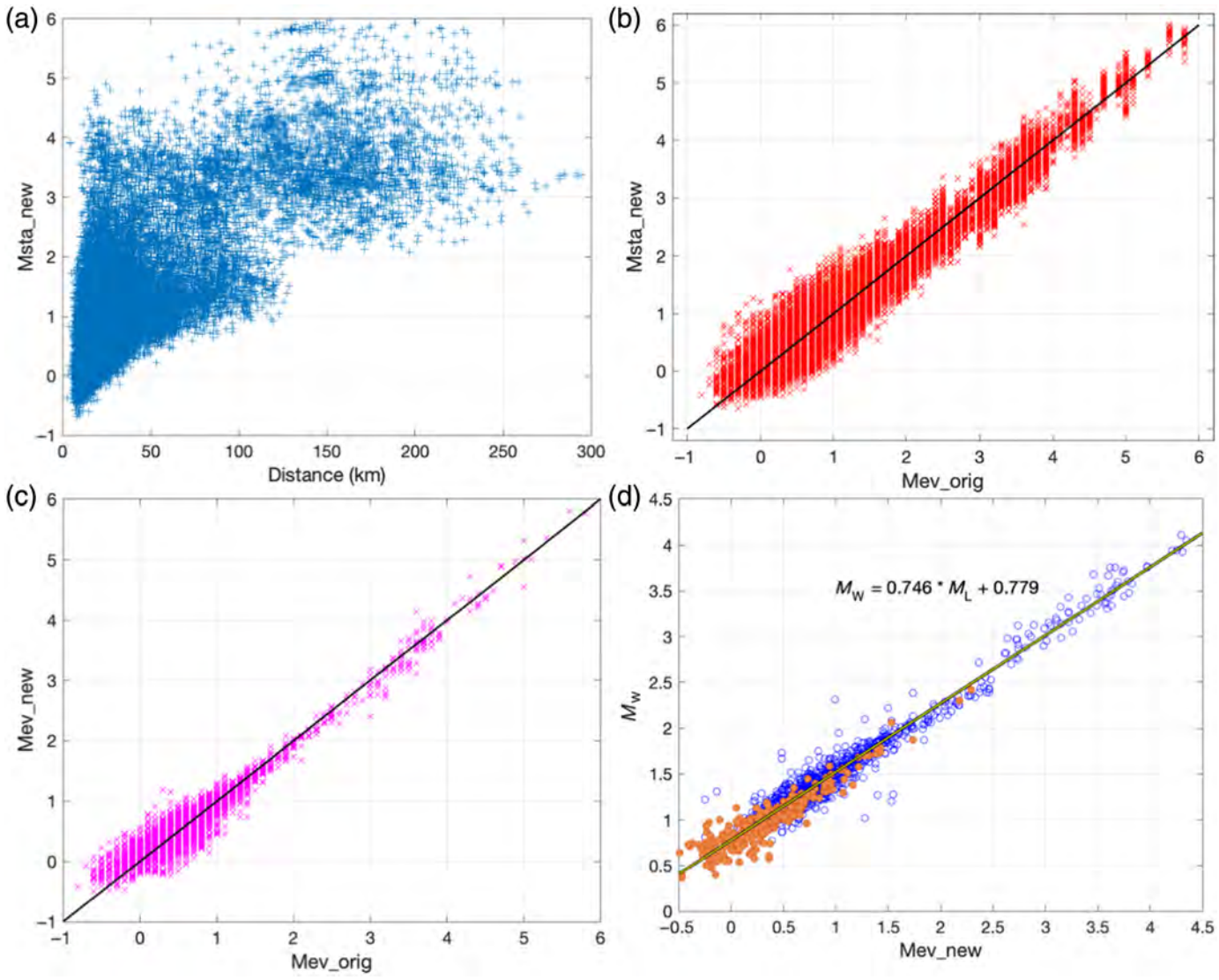

Figure 8. Magnitude comparison plots for the horizontal component (equation 18). (a) Single-station M_L values versus station distances. (b) Single-station M_L values obtained in this study versus the original event–M_Ls. The black line represents the 1:1 identity. (c) Event–M_L values obtained in this study against the original event–M_L. (d) Moment-magnitude M_Ws available for the study area versus event–M_L values obtained in this study; in blue and orange, the values by Tarchini *et al.* (2025) and by Peruzza *et al.* (2022), respectively. The dark, solid line and the equation above it indicate the linear best fit to the data obtained by orthogonal regression. The color version of this figure is available only in the electronic edition.

obtained in this study with the original event–M_L values; the data are well aligned on the diagonal, with a global variability that tends to decrease with magnitude, along with the sample size. This trend is further supported by Figure 8c, which plots the event–M_L values obtained in this study against the original event–M_L values from the dataset. Here, it is clear that the tendency to estimate smaller M_L values becomes more pronounced for events below M_L 2. Finally, Figure 8d illustrates the relationship between the moment magnitude M_w and the new M_L values, both of which are available for some events in the study area. The M_w values are taken from Tarchini *et al.* (2025) for the wide area of NEI, and by Peruzza *et al.* (2022) for a small-magnitude but highly productive seismic sequence that occurred in 2021 near the center of the Collalto network. Note that the available M_w values of Tarchini *et al.* (2025) were calculated uniformly up to a maximum M_w 4.3, and the analyzed time window does not include the main events of the 2012 Emilia sequence. Compared to these two studies, the linear M_w–M_L relationship now obtained by orthogonal regression (OR) (Castellaro and Bormann, 2007) is slightly steeper, but data are less dispersed and feature a more pronounced linear trend in the whole magnitude range. We remind that the OR method is appropriate if the ratio between the errors of the two variables lies between 0.7 and 1.8, a condition that is satisfied by our dataset.

Figure 9 shows the distribution of the station–M_L residuals (single-station M_L minus mean event-M_L) versus hypocentral distance. We use a logarithmic and linear distance scales in panels a and b, respectively because the M_L calibration law

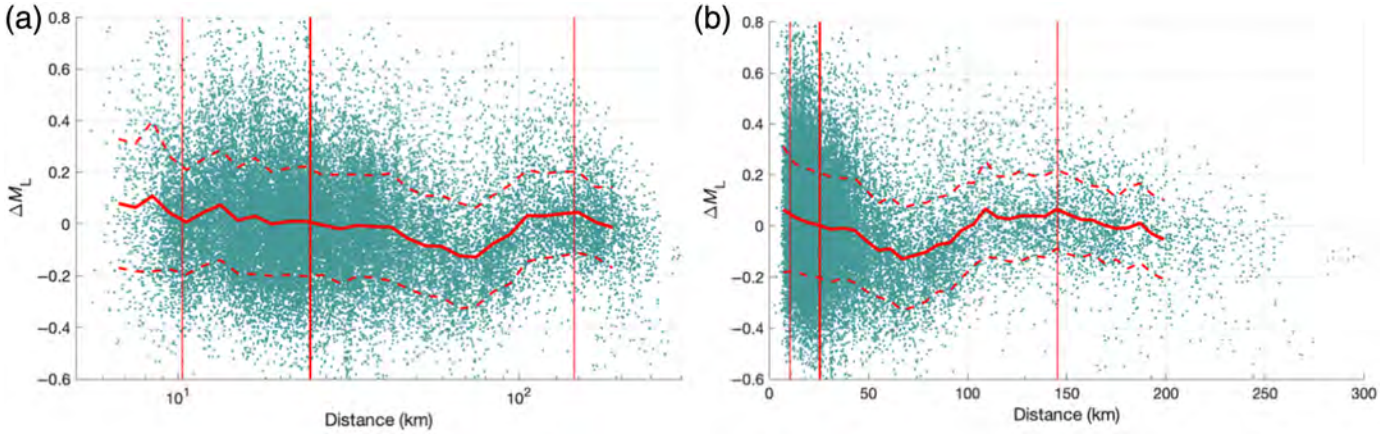

Figure 9. Single-station M_L residuals versus distance for the horizontal component. Panels (a) and (b) show the same data but using logarithmic and linear distance scales, respectively. The thick solid and thin red dashed lines along the distance represent the mean and the mean plus/minus the first standard deviation of the single-station M_L residuals. They are calculated for the logarithmic and linear scale from bins of 0.05 and 6 km, respectively, and represented for the 1st–99th percentile range, that is, 7–205 km. The vertical red lines represent the confidence limit of the 5th percentile, median, and 95th percentile of the distance dataset. The color version of this figure is available only in the electronic edition.

depends on the distance with both the logarithmic terms, which is more sensitive to the short distances, and a linear term that becomes more important at large distances (see also Fig. 5). The average of the residuals is generally around zero, but a clear fluctuation starts at about 40 km, with a negative kink between 40 and 100 km—the minimum being −0.1 at about 65 km—and a positive kink with residual average of about 0.04–0.06 from 100 till about 170 km distance. Slightly positive average residuals, though with small fluctuations, are present in the very short distance range, with values decreasing from about 0.08 at 6–7 km to zero at about 20 km. The standard deviation σ of the residuals is on average of 0.17–0.18. Thus, 0.35 corresponds to 2σ, that is, a confidence value of about 95% that can be taken as a measure of the intraevent variability of the M_Ls estimated by equations (18).

From Figure 9, we can also derive other key elements to assess the validity of the M_L calibration law established in this study. The median hypocentral distance represented is approximately 24.5 km; the minimum and maximum distances are 2.8 and 295 km, respectively. The 5th–95th percentiles range of the distance distribution is 10.5–143.5 km, and the 1st–99th percentile range is 7–205 km (not shown in Fig. 9). Similar values apply to the vertical component.

Based on these results, our equations are valid for distances up to approximately 200 km and magnitudes up to 5.8.

In Figure 10, we compare the M_L equation derived in this study for the horizontal component (equations 18, with $S_i = 0$) with several other equations that are commonly used or relevant to our study. Figure 10a shows the theoretical M_L values calculated by varying the distance for a constant amplitude of 1 mm, and Figure 10b shows the difference between the various equations and that of this study to better visualize the differences in the calibration curves.

Seven equations are compared with the one obtained in this study. These equations are, in order:

- the parametric equation by Bragato and Tento (2005), denoted as BT2005nk, developed for northeastern Italy;
- the nonparametric stepwise law from the same study, denoted as BT2005step;
- the parametric equation (13) by Di Bona (2016), denoted as DB2016, developed for the entire Italian territory;
- the parametric equation by Spallarossa *et al.* (2002), denoted as SBAC2002, calibrated for northwestern Italy;
- the parametric equation by Hutton and Boore (1987), denoted as HB1987, developed for southern California;
- the parametric equation by Butcher *et al.* (2017), denoted as BEtAl2017, which was specifically developed for near-event receivers in the area of New Ollerton town (England) and holds for distances $R \leq 17$ km;
- the parametric equation by Luckett *et al.* (2019), denoted as LEtAl2019, which extended the IASPEI M_L equation (Bormann, 2012) to short distances by incorporating an exponential term, using data from the United Kingdom, central Italy, and Norway.

It should be noted, however, that the equations developed for the Italian territory are used sporadically, and do not represent the common practise for the bulletins published by the various agencies: the INGV national seismic network calculates M_L with the equation HB1987 (Di Maro *et al.*, 2022); the regional networks managed by the University of Genova for northwestern Italy, and by OGS for the northeastern Italy, have adopted duration magnitude since a long time (Bindi *et al.*, 2005; Bragato *et al.*, 2021). The only systematic application of the BT2005nk is done by the Collalto network.

The first notable feature is that, within the validity distance range of this study, the M_L values estimated by equations (18) are, on average, consistent with those derived from the other

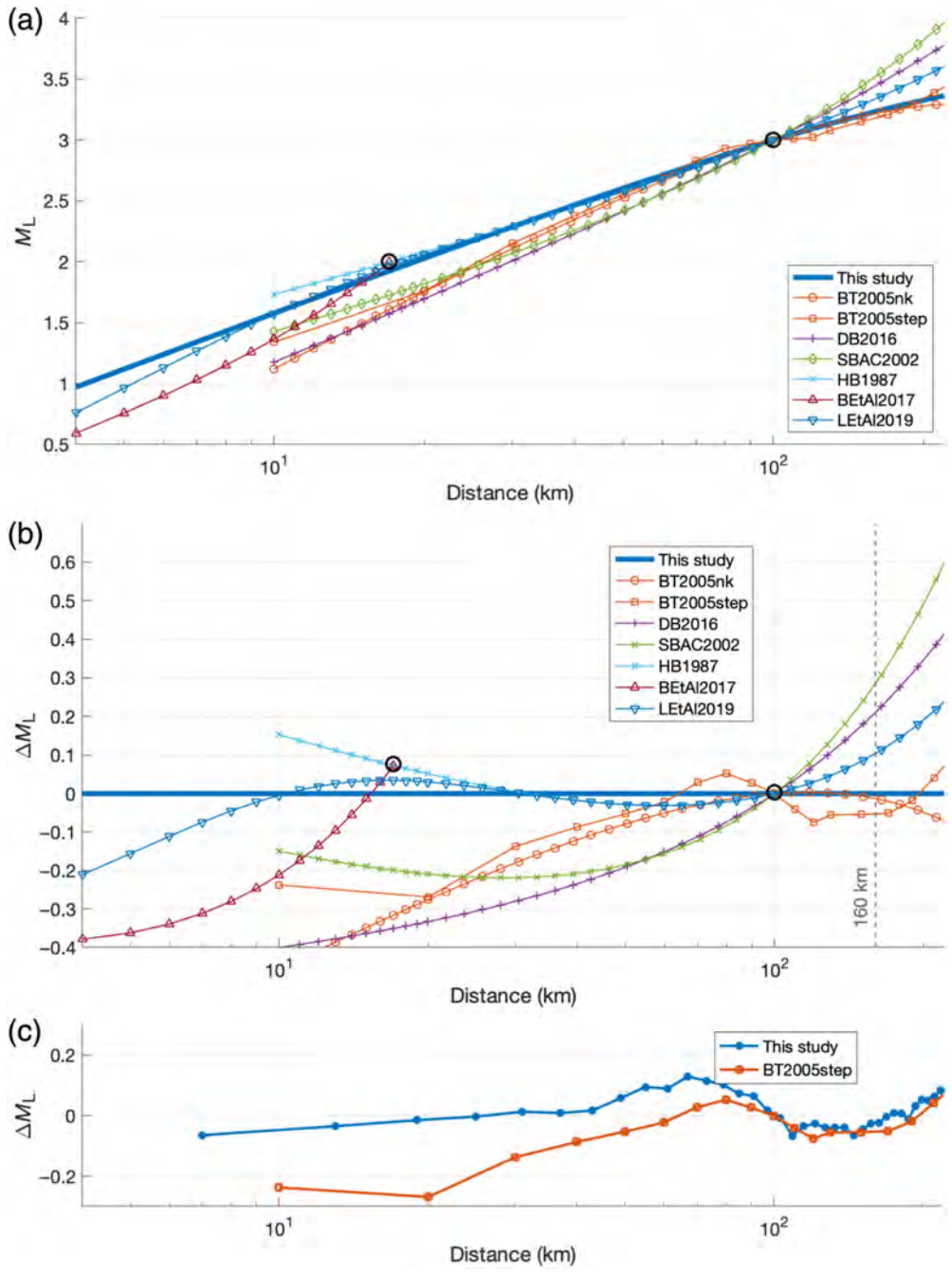

Figure 10. Comparison of the M_L calibration equation of this study with other formulas, labeled as in the main text. (a) M_L corresponding to an amplitude of 1 mm at different distances. (b) Differences between the M_L of this study and the M_Ls of various formulas. (c) Comparison between the average M_L residuals of this study (plotted with the opposite sign from Fig. 9) and the difference between the nonparametric law by Bragato and Tento (2005) and the M_L of this study. The two small black circles in (a) and (b) indicate the calibration points at $R = 100$ km and $M_L = 3$ (original reference set by Richter) and at $R = 17$ km and $M_L = 2$, introduced by Hutton and Boore (1987). For further details, see the text. The color version of this figure is available only in the electronic edition.

equations. Specifically, the maximum variation does not exceed 0.3 for distances of 25–160 km, which is a commonly accepted reference value for the uncertainty in M_L estimation. For distances greater than 160 km, the differences in the calculated M_Ls become more pronounced, in part due to the inversion of the sign of the coefficient K in our equation. The most significant discrepancies at these distances are observed only with the equations by Spallarossa *et al.* (2002) and Di Bona (2016). In contrast, the agreement remains rather strong with the equations by Hutton and Boore (1987) and Luckett *et al.* (2019)—note that these two laws coincide for approximately $R > 30$ km— as well as with those by Bragato and Tento (2005) for $R > 40$ km. In the short-distance range ($R < 15$ km), the M_L values from this study differ by at most approximately −0.15 and −0.35 from the two laws specifically developed for short distances—those by Luckett *et al.* (2019) and Butcher *et al.* (2017) (see Fig. 10a,b).

The comparison with the laws by Bragato and Tento (2005) requires a more detailed discussion. These authors calibrated M_L for an area slightly larger than the one of this study, incorporating several earthquakes to the east, from Slovenia and Croatia, using a different inversion scheme and a dataset entirely independent from the one used in this study. Their records are from the period 1995–2002 (ours from 2012 to 2023) and a smaller number of stations than in our study (25 stations in total, compared to the 41 stations used here). Twelve stations were common to both studies, but, at the time of the study by Bragato and Tento (2005), most were equipped with short-period sensors, instead of broadband sensors and accelerometers. Their study is focused on the regional distances represented by the NEI seismic network, rather than on the short-distance range of the RSC network, and represents a more limited interval of magnitude (0.5–5.2 in Bragato and Tento, 2005, −0.8 to 5.8 in this study).

The n and K coefficients obtained from the initial, global inversion of our new dataset (namely −2.212 and 0.004168 for the horizontal component) are very similar to those of Bragato's parametric curve (−2.23 and 0.0039), including the nonphysical, reverse sign for the K coefficient. Conversely, the final parametric curve obtained from the decimated subsets has remarkably different coefficients (i.e., −1.545 and 0.001357), and is physically more reliable as K approaches zero.

The obtained residuals closely match the deviation of the nonparametric M_L curve of Bragato and Tento (2005) from our law, showing a bump approximately between 40 and 100 km followed by a trough (Fig. 10c). This perturbation of WA amplitudes was attributed to the presence of the Moho discontinuity, the depth of which in northern Italy ranges from 25 to 35 km south of the Alpine chain (Finetti, 2005). We emphasize that the use of a log-linear parametric formulation is essential for identifying a general trend; by quantifying distance-dependent perturbations through the behavior of the residuals, a systematic (i.e., nonrandom) structure may indicate the presence of an underlying physical cause, the nature of which must be investigated independently.

We also note additional advantages of using a parametric law rather than a nonparametric one: a parametric law provides a simple, continuous, and differentiable function of distance, requires only a few coefficients, and avoids possible artificial discontinuities associated with tabular interpolation. Both our parametric law and the nonparametric law of Bragato and Tento exhibit a slight downward bending (Fig. 10a). Despite differences in datasets and inversion formalisms, this consistency suggests that the observed downward bending may reflect a regional feature that should be accounted for in the M_L calibration law. In our approach, the K term is left unconstrained to allow the inversion to best fit the observed dataset, and the resulting solution is well constrained over short-to-intermediate distances (≤200 km). Imposing a hard physical constraint on K (i.e., $K \leq 0$) would alter the n coefficient and degrade the fit in the distance range most relevant for regional M_L calibration, which is inconsistent with the observations. We therefore consider the unconstrained-K approach more suitable for obtaining a globally optimal fit within the applicable distance range. We also find no compelling need to adopt a more complex formulation for the short-distance range. Although Luckett *et al.* (2019) observed that applying the standard equation leads to increased residuals at distances shorter than approximately 15 km, necessitating an additional empirical correction term, our results show that the residuals of the newly calibrated, IASPEI-like equation remain small (mean < 0.1 below 15 km; see Fig. 9a) and do not exhibit any abrupt increase down to 7 km, which we set as the minimum distance validity limit. Furthermore, our calibration curve compares very well with that proposed by Luckett *et al.* (2019) down to 7 km (Fig. 10a,b).

Subsequent studies have provided a more comprehensive understanding of the perturbation of WA amplitudes. Bragato *et al.* (2011) observed that in the Po Plain PGA is systematically enhanced at distances between 70 and 200 km. The authors confirm that this amplification is caused by the reflection of seismic waves at the Moho discontinuity, noting that this effect is "…maximized at hypocentral distances between 90 and 160 km, where the PGA increases by a factor larger than 2.4." Sugan and Vuan (2014) analyze the role of postcritically reflected S waves and multiples from the Moho discontinuity in influencing the ground motion for medium to large earthquakes in northeastern Italy. They demonstrate that high-amplitude *SmSM* phases (Moho reflections and multiples) can be identified within the Po Plain and at the boundaries between the Po Plain and the Alpine chain—thus also affecting northeastern Italy. These phases are observed at epicentral distances greater than 80 km, within a period range of 0.25–3 s, and a group velocity approximately between 2.6 and 3.2 km/s. It is noteworthy that this period partly overlaps with that of the Wood–Anderson seismometer. Di Bona (2016) also points out that his law is suitable for calculating M_L for the entire Italian territory, but "… The only exception is represented by short-distance estimates in northeastern Italy, where increasingly negative residuals for decreasing distances are observed". It is also worth noting that Luckett *et al.* (2019), analyzing the New Ollerton dataset, demonstrated a decrease in local seismic velocities and changes in amplitudes at short distances for very shallow events, thus highlighting variations in the properties of the very shallow crust. We emphasize that our study considers crustal earthquakes with focal depths of at least 4–5 km, corresponding to the upper part of the seismogenic layer in our study area. Detecting similar variations, if present, in a large dataset such as ours would be relevant but would also require a more subtle and demanding analysis, which is beyond the scope of the present work.

We conclude that the pattern of magnitude residuals shown in Figure 10c, independently obtained by Bragato and Tento in 2005, and now by this study, has a physical explanation in the crustal/Moho propagation characteristics.

Another topic worth briefly discussing is the reference distance chosen for the calibration. The original definition was developed for Southern California. In regions with significantly different wave attenuation within the first 100 km, Hutton and Boore (1987) recommend scaling at a 17 km hypocentral distance. This recommendation was adopted by Baumbach *et al.* (2003) for NW Turkey and by Langston *et al.* (1998) for Tanzania. A shift to a shorter reference distance for M_L calibration is indeed justified by the increasing availability of earthquake data at distances less than 100 km, due to the growing number of measurement stations. However, we emphasize that the value of 17 km is tied to the equation of Hutton and Boore (1987) because it corresponds to a Wood–Anderson amplitude of 10 mm at 17 km for an M_L 3 earthquake, or, equivalently, to an amplitude of 1 mm at 17 km for an M_L 2.0 earthquake. If the M_L law changes, the distance at which M_L

decreases by 1 unit below its value at 100 km is no longer 17 km. For example, for the M_L laws shown in Figure 10a, this distance would be approximately 27 km for the law of Spallarossa *et al.* (2002), about 30 km for the law of Di Bona (2016; his equation 13), and roughly 19 km for the law of this study. This can be clearly seen in the M_L law by Butcher *et al.* (2017), which was developed for very near events ($R < 5$ km), was anchored at 17 km, and cannot be applied to larger distances.

Last but not least, the static station coefficients calculated in this study are reported for each documented change in station configuration and are therefore dependent on time and deployment. From Table 2 and Figure S4, we can also observe a reasonably good coherence between the site geology and the static station coefficient: the lower the coefficient, the harder the site or the deeper the sensor deployment. Site geology was taken from Klin *et al.* (2021), in which the site amplification conditions are evaluated by various methods, also in the spectral domain. A thorough investigation of the correlation with the results of that study, as well as of the physical origin of the station corrections (e.g., local geology, very short path effects, site amplification, and their relationship with site response parameters), would require a dedicated, station-focused analysis and potentially additional datasets. Such an analysis is beyond the scope of the present work and will be addressed in a separate, future study.

CONCLUSIONS

We calibrate a local magnitude scale for the area of northeastern Italy, centered around the Collalto seismic network, using the parametric formulation recommended by IASPEI (Bormann *et al.*, 2012) and adopting a modification of the data-driven approach proposed by Chovanová and Kristek (2018). The main aim of the study is to develop an M_L calibration law that is well constrained at short distances for small earthquakes, does not drift for regional distances and moderate earthquakes, and remains consistent with the original Richter definition, using 100 km as the reference distance.

The WA amplitude dataset is derived from digital waveform data collected at 41 stations, between January 2012 and March 2023, referring to more than 3600 earthquakes with magnitudes ranging from −0.8 to 5.8. It includes nearly 35,000 observations for the horizontal component and about 28,000 observations for the vertical component, covering distances between 4 and 295 km.

The parameter values obtained in this study from the simultaneous inversion of the entire dataset are very similar to those reported by Bragato and Tento (2005), who used a different inversion scheme and an independent dataset, although the physical validity of the result is questionable. This similarity suggests that the coefficients may, at least in part, reflect intrinsic characteristics of the study area, as also noted by Di Bona (2016). Nonetheless, we hypothesize that other factors may also influence the inversion results.

We argue that the anomalous coefficient values likely arise from the uneven distribution of data points across distance ranges. To reduce the bias from oversampling, we apply a Monte Carlo-based subsampling approach, generating multiple datasets with more uniform distance distributions by randomly selecting points from the original dataset and performing separate inversions. The final solution, given by equations (18) and (19) for the horizontal and vertical components, expresses amplitudes in millimeters and includes static station coefficients that vary over time with station configuration. These equations are valid for distances of 7–200 km and magnitudes of −0.8 to 5.8. The static station coefficients are consistent with expectations (Bormann, 2012), remaining within ±0.6, and show reasonably good coherence with site geology and deployment modality.

The M_L equation derived here is, on average, consistent with other equations commonly used or relevant to our study area; in particular, it is close to the formula proposed by Hutton and Boore (1987) in the distance range 15–160 km, with M_L differences lower than 0.1. It is worth noting, however, that in the short-distance range ($R < 15$ km), which is the primary focus of this study, the curves by Luckett *et al.* (2019) and Butcher *et al.* (2017) provide lower values than ours, whereas that by Hutton and Boore (1987) overestimates the magnitude compared with ours. For distances below 25 km, the formulas (both parametric and nonparametric) of Bragato and Tento (2005), which were developed for the same area, also yield magnitude values that are at least 0.2 lower than ours. At distances of about 50–200 km, the average M_L residuals of our parametric law confirm the perturbation of WA amplitudes for which systematic (i.e., nonrandom) structure is attributed to the presence of the Moho discontinuity.

Finally, in the magnitude range −0.5 to 4.3, our M_L law exhibits a strong linear relationship with the available M_w values, and is less affected by the systematic drift that appears at low magnitudes when compared with other laws. This suggests that our new law provides a more accurate estimate of earthquake energy across the entire range analyzed.

Our new calibration scale provides reliable M_L estimates in northeastern Italy, even at short distances, while maintaining coherence with the standard IASPEI formula. It is also suitable for consistent application, accommodating observations from both dense local networks and regional networks. Thus, it is suitable for local magnitude estimation in the whole area of northeastern Italy.

DATA AND RESOURCES

The earthquake catalog used in this study is available upon request to the authors. The complete catalog of the northeast Italy (NEI) network by the National Institute of Oceanography and Applied Geophysics (OGS) can be found at https://terremoti.ogs.it/ (last accessed March 2025). Continuous waveform data of NEI (OGS) and RSN (INGV) networks are available at European Integrated Data Archive (EIDA): https://eida.ingv.it/it/ (last accessed February 2025). Information and data on

the Collalto seismic network (RSC) can be found at http://rete-collalto.crs.inogs.it (last accessed February 2025). Seismic data of the RSC are acquired and processed using the BRTT Antelope system at http://www.brtt.com/ (last accessed March 2025), supplemented by some procedures and functions developed by OGS staff. The unique identifiers (e.g., channel convention) for data sources exchanged and archived in formats and services defined by the International Federation of Digital Seismograph Networks are described at http://docs.fdsn.org/projects/source-identifiers/en/v1.0/ (last accessed February 2025). The poles and zeros file (.paz) for simulating the Wood–Anderson response is provided by the EarthScope Data Services (DS) at the following link: https://ds.iris.edu/pipermail/sac-help/2013-March/001430.html (last accessed March 2025). The following software systems were used: Seismic Analysis Code (SAC) (Version 102.0, 2020; Goldstein *et al.*, 2003 and Helffrich *et al.*, 2013) available at http://ds.iris.edu/ds/nodes/dmc/software/downloads/sac/ (last accessed March 2025); GNU Awk (gawk) version 4.2.0 (Free Software Foundation), with its GNU implementation GAWK at: www.gnu.org/software/gawk (last accessed August 2021); and MATLAB, versions R2018b and 2019b, Natick, Massachusetts: The MathWorks Inc. at https://www.mathworks.com/products/matlab.html (last accessed November 2025), Hypo71 at https://pubs.usgs.gov/publication/ofr72224 (last accessed March 2025), and HYPOELLIPSE https://pubs.usgs.gov/of/1999/ofr-99-0023/ (last accessed March 2025). The MATLAB code was used to implement the whole method of magnitude calibration as proposed by Chovanová and Kristek (2018), the additional step to reduce the bias caused by data oversampling along distance, and all Figures from 2 to 10. Maps of Figure 1 have been created using the free and open-source QGIS. This article is accompanied by supplemental material. The supplemental material for this article contains five text sections. Text S1 describes the synthetic tests performed to verify the MATLAB code used in our study, which implements the method of Chovanová and Kristek (2018). Text S2 summarizes the instrumental settings of the stations, the station subcodes associated with each configuration, and the static station correction coefficients obtained after magnitude calibration. Text S3 presents a sensitivity analysis of the effect of an incorrect hypocentral location on M_L estimation. Text S4 details the sensitivity analysis of the impact of the band-pass filter on large earthquakes. Text S5 reports the amplitude ratio estimated between the horizontal and vertical components.

DECLARATION OF COMPETING INTERESTS

The authors acknowledge that there are no conflicts of interest recorded.

ACKNOWLEDGMENTS

This study was carried out within the RETURN Extended Partnership and received funding from the European Union Next-GenerationEU (National Recovery and Resilience Plan—NRRP, Mission 4, Component 2, Investment 1.3—D. D. 1243 2 August 2022, PE0000005). This study has used data acquired by the seismic networks managed by the National Institute of Oceanography and Geophysics (OGS), the National Institute of Geophysics and Volcanology (INGV), and the Geological Survey of the Provincia Autonoma di Trento. The regional networks of OGS are managed and supported within agreements with the Civil Protection of the Regione Autonoma Friuli Venezia Giulia and Regione Veneto; the network of Collalto is managed by OGS within an agreement with Edison Stoccaggio S.p.a, a society of EDF group recently acquired by Snam through its subsidiary Stogit Adriatica S.p.a. The authors thank the technical staff of the Centro Ricerche Sismologiche (CRS-OGS) for the management of these networks and the data acquired by them.

The authors are grateful to the Editor and the four reviewers, in particular Reviewer 2 (anonymous) and 3 (Paolo Gasperini), for their constructive and thorough comments, which greatly improved this article. The authors also thank Luca Moratto of OGS for the M_w data of the Refrontolo seismic sequence of 2021, which are represented in Figure 8.

REFERENCES

Anderlini, L., E. Serpelloni, C. Tolomei, P. M. De Martini, G. Pezzo, A. Gualandi, and G. Spada (2020). New insights into active tectonics and seismogenic potential of the Italian Southern Alps from vertical geodetic velocities, *Solid Earth* **11,** 1681–1698, doi: 10.5194/se-11-1681-2020.

Bakun, W. H., and W. B. Joyner (1984). The ML scale in central California, *Bull. Seismol. Soc. Am.* **74,** 1827–1843, doi: 10.1785/BSSA0740051827.

Baumbach, M., D. Bindi, H. Grosser, C. Milkereit, S. Parolai, R. Wang, S. Karakisa, S. Zünbül, and J. Zschau (2003). Calibration of an ML scale in northwestern Turkey from 1999 Izmit aftershocks, *Bull. Seismol. Soc. Am.* **93,** 2289–2295, doi: 10.1785/0120020157.

Bindi, D., D. Spallarossa, C. Eva, and M. Cattaneo (2005). Local and duration magnitudes in northwestern Italy, and seismic moment versus magnitude relationships, *Bull. Seismol. Soc. Am.* **95,** 592–604, doi: 10.1785/0120040099.

Bobbio, A., M. Vassallo, and G. Festa (2009). A local magnitude scale for southern Italy, *Bull. Seismol. Soc. Am.* **99,** 2461–2470, doi: 10.1785/0120080364.

Bommer, J. J., S. Oates, J. M. Cepeda, C. Lindholm, J. Bird, R. Torres, G. Marroquín, and J. Rivas (2006). Control of hazard due to seismicity induced by a hot fractured rock geothermal project, *Eng. Geol.* **83,** 287–306, doi: 10.1016/j.enggeo.2005.11.002.

Bormann, P. (Editor) (2012). *New Manual of Seismological Observatory Practice (NMSOP-2)*, IASPEI, GFZ German Research Centre for Geosciences, Potsdam.

Bormann, P., J. Dewey, and , and the IASPEI/CoSOI Working Group on Magnitude Measurement (2012). The new IASPEI standards for determining magnitudes from digital data and their relation to classical magnitudes, Information Sheet 3.3, in *New Manual of Seismological Observatory Practice (NMSOP-2)*, P. Bormann (Editor), IASPEI, GFZ German Research Centre for Geosciences, Potsdam, 44 pp.

Bragato, P. L., and A. Tento (2005). Local magnitude in northeastern Italy, *Bull. Seismol. Soc. Am.* **95,** no. 2, 579–591, doi: 10.1785/0120040100.

Bragato, P. L., P. Comelli, A. Saraò, D. Zuliani, L. Moratto, V. Poggi, G. Rossi, C. Scaini, M. Sugan, C. Barnaba, *et al.* (2021). The OGS-northeastern Italy seismic and deformation network: Current status and outlook, *Seismol. Res. Lett.* **93,** no. 3, 1704–1716, doi: 10.1785/0220200372.

Bragato, P.L., M. Sugan, P. Augliera, M. Massa, A. Vuan, and A. Saraò (2011). Moho reflection effects in the Po plain (northern Italy) observed from instrumental and intensity data, *Bull. Seismol. Soc. Am.* **101,** no. 5, 2142–2152, doi: 10.1785/0120100257.

Butcher, A., R. Luckett, J. Verdon, M. Kendall, B. Baptie, and J. Wookey (2017). Local magnitude discrepancies for near-event

receivers: Implications for the UK traffic-light scheme, *Bull. Seismol. Soc. Am.* **107,** no. 2, 532–541, doi: 10.1785/0120160225.

Castellaro, S., and P. Bormann (2007). Performance of different regression procedures on the magnitude conversion problem, *Bull. Seismol. Soc. Am.* **97,** no. 4, 1167–1175, doi: 10.1785/0120060102.

Chovanová, Z., and J. Kristek (2018). A local magnitude scale for Slovakia, Central Europe, *Bull. Seismol. Soc. Am.* **108,** no. 5A, 2756–2763, doi: 10.1785/0120180059.

Di Bona, M. (2016). A local magnitude scale for crustal earthquakes in Italy, *Bull. Seismol. Soc. Am.* **106,** 242–258, doi: 10.1785/0120150155.

Di Maro, R., L. Arcoraci, P. Battelli, M. Berardi, C. Castellano, B. Castello, D. Latorre, A. Marchetti, L. Margheriti, F. Mele, *et al.* (2022). Bollettino Sismico Italiano 2015, *Quad. Geofis.* **176,** 1–52, doi: 10.13127/qdg/176.

Finetti, I. R. (2005). Crustal tectono-stratigraphic sections across the western and eastern Alps from ECORS-CROP and Transalp seismic data, in *CROP Project: Deep Seismic Exploration of the Central Mediterranean and Italy*, Vol. 7, Elsevier Science and Technology, Amsterdam, The Netherlands, 109–117.

Gentili, S., M. Sugan, L. Peruzza, and D. Schorlemmer (2011). Probabilistic completeness assessment of the past 30 years of seismic monitoring in northeastern Italy, *Phys. Earth Planet. In.* **186,** 81–96, doi: 10.1016/j.pepi.2011.03.005.

Goldstein, P., D. Dodge, and M. Firpo (2003). SAC2000: Signal processing and analysis tools for seismologists and engineers, Incorporated Research Institutions for Seismology (IRIS).

Havskov, J., and L. Ottenmöller (2010). *Routine Data Processing in Earthquake Seismology*, Springer, 347 pp., doi: 10.1007/978-90-481-8697-6.

Helffrich, G., J. Wookey, and I. Bastow (2013). *The Seismic Analysis Code. A Primer and User's Guide*, Cambridge University Press, doi: 10.1017/CBO9781139547260.

Husen, S., and J. L. Hardebeck (2010). Earthquake location accuracy, *Community Online Resource for Statistical Seismicity Analysis*, doi: 10.5078/corssa-55815573.

Hutton, L., and D. M. Boore (1987). The ML scale in southern California, *Bull. Seismol. Soc. Am.* **77,** 2074–2094, doi: 10.1785/BSSA0770062074.

Incorporated Research Institutions for Seismology (IRIS) (2012). SEED reference manual: Standard for the exchange of earthquake data, Incorporated Research Institutions for Seismology – IRIS, available at https://www.fdsn.org/pdf/SEEDManual_V2.4.pdf (last accessed March 2025).

Klin, P., G. Laurenzano, C. Barnaba, E. Priolo, and S. Parolai (2021). Site amplification at permanent stations in northeastern Italy, *Bull. Seismol. Soc. Am.* **111,** 1885–1904, doi: 10.1785/0120200361.

Lahr, J. (1999). HYPOELLIPSE: A computer program for determining local earthquake hypocentral parameters, magnitude, and first-motion pattern, *U.S. Geol. Surv. Open-File Rept. 99-23*, available at http://pubs.usgs.gov/of/1999/ofr-99-0023 (last accessed March 2025).

Langston, C. A., R. Brazier, A. A. Nyblade, and T. J. Owens (1998). Local magnitude scale and seismicity rate for Tanzania, East Africa, *Bull. Seismol. Soc. Am.* **88,** no. 3, 712–721, doi: 10.1785/BSSA0880030712.

Lee, W. H. K., and J. C. Lahr (1975). HYP071 (Revised): A computer pro- gram for determining hypocenter, magnitude and first-motion pattern of local earthquakes, *U.S. Geol. Surv. Open-File Rept. 75-311*, doi: 10.3133/ofr75311.

Lolli, B., P. Gasperini, and F. Mele (2015), Recalibration of the distance correction term for local magnitude (ML) computations in Italy, *Seismol. Res. Lett.* **86,** 1383–1391, doi: 10.1785/0220150020.

Luckett, R., L. Ottemöller, A. Butcher, and B. Baptie (2019). Extending local magnitude M_L to short distances, *Geophys. J. Int.* **216,** no. 2, 1145–1156, doi: 10.1093/gji/ggy484.

Majer, E., J. Nelson, A. Robertson-Tait, J. Savy, and I. Wong (2012). Protocol for addressing induced seismicity associated with enhanced geothermal systems, *DOE/EE-0662*, U.S. Department of Energy.

Maury, J., M. Peter-Borie, P. Dominique, F. De Santis, E. Klein, and I. Contrucci (2023). Guide de bonnes pratiques pour la maîtrise de la sismicité induite par les opérations de géothermie profonde, BRGM Éditions, available at https://www.ecologie.gouv.fr/sites/default/files/documents/Guide-geothermie.pdf (last accessed September 2024).

Michelini, A., L. Margheriti, M. Cattaneo, G. Cecere, G. D'Anna, A. Delladio, M. Moretti, S. Pintore, A. Amato, A. Basili, *et al.* (2016). The Italian National Seismic Network and the earthquake and tsunami monitoring and surveillance systems, *Adv. Geosci.* **43,** 31–38, doi: 10.5194/adgeo-43-31-2016.

MiSE-UNMIG (2014). Guidelines for monitoring seismicity, ground deformation and pore pressure in subsurface industrial activities, Ministero per lo Sviluppo Economico (MiSE)—Ufficio nazionale minerario per gli idrocarburi e le georisorse (UNMIG), available at https://unmig.mase.gov.it/geomonitoraggi/linee-guida-per-i-monitoraggi/ (last accessed March 2025).

Moratto, L., A. Saraò, and E. Priolo (2017). Moment magnitude (Mw) estimation of weak seismicity in Northeastern Italy, *Seismol. Res. Lett.* **88,** 1455–1464, doi: 10.1785/0220170063.

Ottenmöller, L., and S. Sargeant (2013). A local magnitude scale ML for the United Kingdom, *Bull. Seismol. Soc. Am.* **103,** 2884–2893, doi: 10.1785/0120130085.

Peresan, A., and S. Gentili (2018). Seismic clusters analysis in northeastern Italy by the nearest-neighbor approach, *Phys. Earth Planet. In.* **274,** 87–104, doi: 10.1016/j.pepi.2017.11.007.

Peruzza, L., M. A. Romano, M. Guidarelli, L. Moratto, M. Garbin, and E. Priolo (2022). An unusually productive microearthquake sequence brings new insights to the buried active thrust system of Montello (southeastern Alps, northern Italy), *Front. Earth Sci.* **10,** doi: 10.3389/feart.2022.1044296.

Picotti, V., M. A. Romano, A. Ponza, F. L. Guido, and L. Peruzza (2022). The Montello thrust and the active mountain front of the eastern southern Alps (northeast Italy), *Tectonics* **41,** doi: 10.1029/2022TC007522.

Priolo, E., C. Barnaba, P. Bernardi, G. Bernardis, P. L. Bragato, G. Bressan, M. Candido, E. Cazzador, P. Di Bartolomeo, G. Durì, *et al.* (2005). Seismic monitoring in northeastern Italy: A ten-year experience, *Seismol. Res. Lett.* **76,** no. 4, 446–454, doi: 10.1785/gssrl.76.4.446.

Priolo, E., M. Romanelli, M. P. Plasencia Linares, M. Garbin, L. Peruzza, M. A. Romano, P. Marotta, P. Bernardi, L. Moratto, D. Zuliani, *et al.* (2015). Seismic monitoring of an underground natural gas storage facility: The Collalto Seismic Network, *Seismol. Res. Lett.* **86,** 109–123, doi: 10.1785/0220140087.

Richter, C. F. (1935). An instrumental earthquake magnitude scale, *Bull. Seismol. Soc. Am.* **25,** 1–32.

Richter, C. F. (1958). *Elementary Seismology*, W. H. Freeman, San Francisco, California, 578 pp.

Romano, M. A., L. Peruzza, M. Garbin, E. Priolo, and V. Picotti (2019). Microseismic portrait of the Montello thrust (southeastern Alps, Italy) from a dense, high-quality seismic network, *Seismol. Res. Lett.* **90,** 1502–1517, doi: 10.1785/0220180387.

Rovida, A., M. Locati, R. Camassi, B. Lolli, and P. Gasperini (2020). The Italian earthquake catalogue CPTI15, *Bull. Earthq. Eng.* **18,** no. 7, 2953–2984, doi: 10.1007/s10518-020-00818-y.

Rovida, A., M. Locati, R. Camassi, B. Lolli, P. Gasperini, and A. Antonucci (2022). Catalogo Parametrico dei Terremoti Italiani (CPTI15), versione 4.0 [Data set], *Istituto Nazionale di Geofisica e Vulcanologia (INGV)*, doi: 10.13127/cpti/cpti15.4.

Sandron, D., A. Rebez, and D. Slejko (2018). Calibration of the duration magnitude for the north-eastern Italy seismometric network (OX) on the basis of the revised local magnitudes of the Trieste station, *Bull. Geofis. Teor. Appl.* **59,** no. 3, 249–266, doi: 10.4430/bgta0237.

Spallarossa, D., D. Bindi, P. Augliera, and M. Cattaneo (2002). An ML scale in northwestern Italy, *Bull. Seismol. Soc. Am.* **92,** 2205–2216, doi: 10.1785/0120010201.

Sugan, M., and A. Vuan (2014). On the ability of Moho reflections to affect the ground motion in northeastern Italy: A case study of the 2012 Emilia seismic sequence, *Bull. Earthq. Eng.* **12,** 2179–2194, doi: 10.1007/s10518-013-9564-y.

Sugan, M., A. Saraò, A. Magrin, A. Snidarcig, G. Bressan, G. Renner, M. A. Romano, M. Guidarelli, M. Santulin, P. Di Bartolomeo, *et al.* (2024). Focal mechanisms of the southeastern Alps and surroundings (2.0) [Data set], *Zenodo*, doi: 10.5281/zenodo.10853582.

Tarchini, G., L. Moratto, and A. Saraò (2025). A comprehensive moment magnitude catalog for the northeastern Italy region, *Seismol. Res. Lett.* **96,** no. 4, 2714–2723, doi: 10.1785/0220240303.

Uhrhammer, R. A., and E. R. Collins (1990). Synthesis of Wood–Anderson seismograms from broadband digital records, *Bull. Seismol. Soc. Am.* **80,** 702–716.

Manuscript received 21 March 2025
Published online 12 March 2026